

Inverse Problems in Astronomical Adaptive Optics

B L Ellerbroek¹ and C R Vogel²

¹Thirty Meter Telescope Project, Pasadena, CA, USA

² Department of Mathematical Sciences, Montana State University, Bozeman, MT 59717-2400 USA

E-mail: brente@caltech.edu, vogel@math.montana.edu

Abstract. Adaptive optics (AO) is a technology used in ground-based astronomy to correct for the wavefront aberrations and loss of image quality caused by atmospheric turbulence. Provided some difficult technical problems can be overcome, AO will enable future astronomers to achieve nearly diffraction-limited performance with the extremely large telescopes that are currently under development, thereby greatly improving spatial resolution, spectral resolution, and observing efficiency which will be achieved. The goal of this topical review is to present to the Inverse Problems community a representative sample of these problems. In this article we first present a tutorial overview of the mathematical models and techniques used in current AO systems. We then examine in detail the following topics: laser guidestar adaptive optics; multi-conjugate and multi-object adaptive optics; high-contrast imaging; and deformable mirror modeling and parameter identification.

1. Introduction

The term *adaptive optics* (AO) refers to optical systems that adapt in real time to compensate for distorting effects introduced along the propagation path between a light source and a receiver. In ground-based astronomy, light from distant objects is distorted by the effects of turbulence as it propagates through the earth’s atmosphere. This leads to severe degradation in the quality of images that can be obtained with a telescope. The purpose of AO in astronomy is to physically compensate for these distortions, thereby greatly improving image quality.

The limitations imposed by atmospheric turbulence upon astronomical image quality have been recognized for centuries [47]. The possibility of correcting for atmospheric effects using some to-be-determined method was hypothesized at least as early as 1908 [31]. Babcock [4] is generally given credit for the first demonstration of adaptive optics on an astronomical telescope in the early 1950’s, although the technology available at the time limited the system to first-order image motion compensation. Advances in optical detectors, materials, and computers led to sustained interest in AO and a range of more ambitious demonstrations in the 1970’s [34], and the first path finder systems for small, astronomical telescopes were successfully deployed in the late 1980’s and early 1990’s [35]. AO systems are now in regular use at most, if not all, members of the current generation of large astronomical telescopes, where they have been used for observations and discoveries including imaging of the Galilean moons of Jupiter [44], measuring the mass of the black hole at the center of the Milky Way galaxy (see Fig. 1) via precise measurement of the orbits of co-located stars [22], and the direct detection (i.e. direct imaging) of extra-solar planets in orbit around nearby stars [45]. For the future, AO is also considered to be essential to the “sciences cases” for the next generation of so-called extremely-large telescopes now under development [61, 28, 16].

The goal of this topical review article is to provide an overview of the field of astronomical AO to the Inverse Problems community. For the benefit of those with limited AO expertise, we begin with a brief tutorial in section 2, outlining the basic principles and components of an astronomical AO system. This includes mathematical models for image formation, atmospheric light wave propagation, and atmospheric turbulence. It also includes models for the wavefront sensors used to detect the effects of turbulence and the deformable mirrors used to correct for these effects. In this tutorial we also introduce the wavefront reconstructor, an AO subsystem which maps sensor measurements to commands that drive the actuators of the deformable mirrors. At the end of the tutorial, we address the following important question: Why apply AO when one might simply form an image with a conventional telescope and then enhance the image using deconvolution?

We will then discuss in greater detail a few of the current research topics that we believe to be important and relevant to experts on Inverse Problems. Section 3 covers laser guidestar AO. Laser guidestars provide light needed to drive the wavefront sensors in an astronomical AO system, but they introduce certain complications that do not arise when (often inadequate) light from naturally occurring stars is used. In this section we address sensor modeling issues and present solutions to some of the problems that arise in laser guidestar AO.

In section 4 we discuss complex AO systems that combine information from both natural and laser guidestars and make use of multiple deformable mirrors for wavefront correction. We analyze the mathematical structure of the wavefront reconstructors

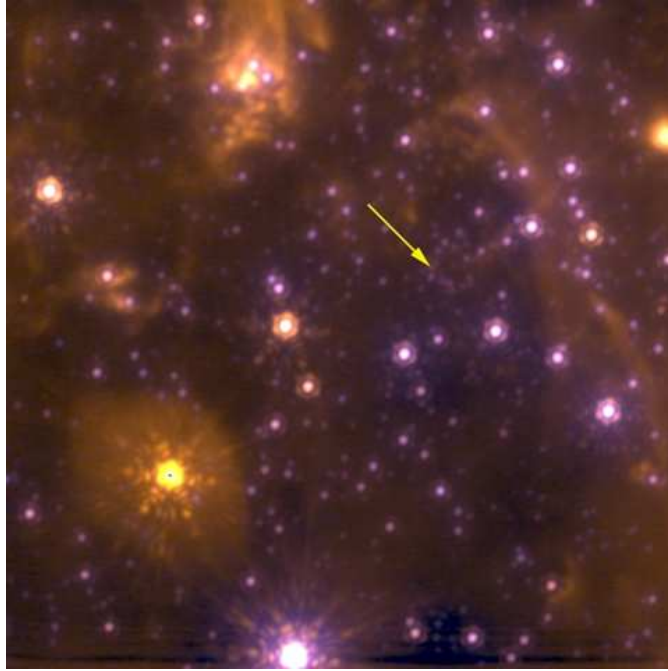


Figure 1. Narrow-field image of the Galactic Center, taken with the Keck Telescope. The arrow marks the location of radio source Sgr A*, a supermassive black hole at the center of our galaxy.

for such systems and we discuss in the detail the numerical implementation of these reconstructors.

In section 5 we introduce more complex deformable mirror models and we present techniques that can be used to estimate relevant parameters in these models. This is important for certain proposed concepts in future AO systems that will need to operate in “open loop”, i.e., without direct feedback.

The topic of section 6 is AO for high-contrast imaging. We review one of the techniques (Lyot coronagraphy) which has been proposed for the extremely difficult task of directly imaging planets orbiting around neighboring stars, and we discuss the modeling and computational issues that arise from this technique.

There are a number of important and mathematically interesting topics in astronomical AO that are beyond the scope of this article. Of particular importance in high-contrast imaging is the estimation of (temporal) dynamics of atmospheric turbulence from wavefront sensor measurements [51]. AO image post processing, and in particular, the modeling and parameter estimation of the point spread functions which arise from AO imaging systems [21] is also not discussed. We will also not cover innovative wavefront sensing and estimation techniques like pyramid sensing [10] and phase diversity [48].

Also not directly addressed in this review article are other important applications of AO, including laser communications [30], imaging of the retina of the eye [9], and consumer electronics [11]. Certain topics from this paper, like wavefront sensing and deformable mirrors, do pertain to these applications. However, each application has unique features which require specialized techniques. For instance, in high-resolution

imaging of the retina using AO, the estimation of the motion of the eye is of critical importance [64].

The literature cited in this review is extensive, but by no means comprehensive. Interested readers may peruse textbooks by Hardy [32], Roddier [53], and Roggemann and Welsh [54] for a more thorough review of the literature in astronomical AO through the late 1990s. We apologize to authors of more recent important work that we fail to cite.

Before proceeding with the tutorial, we present some of the mathematical notation that will be used throughout this review.

1.1. Notation

We denote position in 3-d space by $\mathbf{x} = (x, y, z)$. Omitting the vertical component z gives us 2-d position. The 2-d Fourier transform operator is given by

$$\mathcal{F}\{f\}(u, v) = \int_{-\infty}^{\infty} \int_{-\infty}^{\infty} f(x, y) e^{-i2\pi(xu+yv)} dx dy, \quad (1.1)$$

where $i = \sqrt{-1}$. Variables u and v are the components of 2-d spatial frequency and have physical units of inverse length.

To model atmospheric turbulence, we will rely on random functions, or stochastic processes. In this context a random function $f = f(\mathbf{x}, \omega)$, where ω lies in a probability space, has either the real numbers or the complex numbers as its range. For notational convenience, we typically omit dependence on ω . For each fixed \mathbf{x} , we obtain a random variable whose mean is given by

$$\bar{f}(\mathbf{x}) = \langle f(\mathbf{x}) \rangle, \quad (1.2)$$

where $\langle \cdot \rangle$ denotes expected value, or ensemble average. The covariance of f is defined by

$$C_f(\mathbf{x}, \mathbf{x}') = \langle (f(\mathbf{x}) - \bar{f}(\mathbf{x}))(f(\mathbf{x}') - \bar{f}(\mathbf{x}')) \rangle. \quad (1.3)$$

f is called *strictly stationary* if it has constant mean and its covariance function depends only the spatial separation $\Delta\mathbf{x} = \mathbf{x} - \mathbf{x}'$.

We will also make use of basic concepts from the calculus of variations. Let \mathcal{F} denote a Hilbert space with inner product (\cdot, \cdot) and corresponding norm

$$\|f\| \stackrel{\text{def}}{=} \sqrt{(f, f)}, \quad f \in \mathcal{F}. \quad (1.4)$$

Of primary interest is the standard L^2 inner product

$$(f, g)_{L^2(\Omega)} = \int_{\Omega} f(\mathbf{x}) g(\mathbf{x}) d\mathbf{x},$$

where Ω is a closed and bounded region in 2- or 3-dimensional space. Let J be a real-valued function defined on \mathcal{F} . The directional derivative of J at $f \in \mathcal{F}$ in the direction $h \in \mathcal{F}$ is given by

$$DJ(f; h) \stackrel{\text{def}}{=} \lim_{\tau \rightarrow 0} \frac{J(f + \tau h) - J(f)}{\tau} \quad (1.5)$$

The gradient g of J at f , if it exists, is characterized by

$$DJ(f; h) = (g, h), \quad \text{for all } h \in \mathcal{F}. \quad (1.6)$$

In case \mathcal{F} is the n -dimensional Euclidean space \mathbf{R}^n , we use standard notation for the components of the gradient of J at $\mathbf{f} = (f_1, \dots, f_n)$,

$$[\nabla J]_i = \frac{\partial J}{\partial f_i} = J_{f_i}, \quad i = 1, \dots, n.$$

We will employ notation analogous to (1.5) for the Gateaux derivative of a possibly nonlinear operator $A : \mathcal{F} \rightarrow \mathcal{G}$, where \mathcal{G} is a second Hilbert space,

$$DA(f; h) \stackrel{\text{def}}{=} \lim_{\tau \rightarrow 0} \frac{A(f + \tau h) - A(f)}{\tau}. \quad (1.7)$$

If $A(\alpha f + \beta h) = \alpha A f + \beta A h$ for all scalars α, β and all $f, h \in \mathcal{F}$, then A is linear and

$$DA(f; h) = A h,$$

independent of $f \in \mathcal{F}$. If in addition,

$$(A f, h) = (f, A h) \quad \text{for all } f, h \in \mathcal{F}, \quad (1.8)$$

then A is called a *self-adjoint* linear operator.

Our development of wavefront reconstructors in section 2.7 will rely on the trace norm on the Hilbert space of square-integrable random vectors which have zero mean,

$$\langle \| \mathbf{f} \|^2 \rangle = \left\langle \sum_{i=1}^n f_i^2 \right\rangle = \sum_{i=1}^n [C_{\mathbf{f}}]_{ii} \stackrel{\text{def}}{=} \text{trace } C_{\mathbf{f}}, \quad (1.9)$$

where $C_{\mathbf{f}}$ denotes the covariance matrix for the random vector \mathbf{f} .

Finally, we will abbreviate “right-hand-side” and “left-hand-side” by RHS and LHS, respectively; for instance, $DJ(f; h)$ appears on the LHS of Eq. (1.6).

2. A Brief Tutorial on Atmospheric Adaptive Optics

A conventional AO system requires the following components: (i) a corrective element such as a deformable mirror to flatten the aberrated wavefronts; (ii) a device known as a wavefront sensor to measure the aberrations; (iii) a light source to drive the sensor; and (iv) a subsystem known as a wavefront reconstructor, which takes in sensor measurements and produces “commands” for the corrective elements, e.g., deformable mirror actuator voltages. See the diagram in Fig. 2.

Before we introduce mathematical models for the components of the AO system, we briefly discuss the image formation process itself.

2.1. Basics of Optical Image Formation.

We begin with an isoplanatic Fourier optics model [29] for a simple telescope, which relates the image I to the object f ,

$$I(u, v) = \int_{-\infty}^{\infty} \int_{-\infty}^{\infty} s_{\phi}(u - u', v - v') f(u', v') du' dv', \quad (2.10)$$

where the point spread function (PSF) s_{ϕ} can be represented as

$$s_{\phi}(u, v) = |\mathcal{F}\{A e^{i\phi}\}(u, v)|^2. \quad (2.11)$$

Here $A = A(x, y)$ is the aperture function. Neglecting amplitude variations, this takes a value of one within the telescope aperture (a disk or possibly a more general two-dimensional domain) and is zero outside this domain. (x, y) denotes position in the

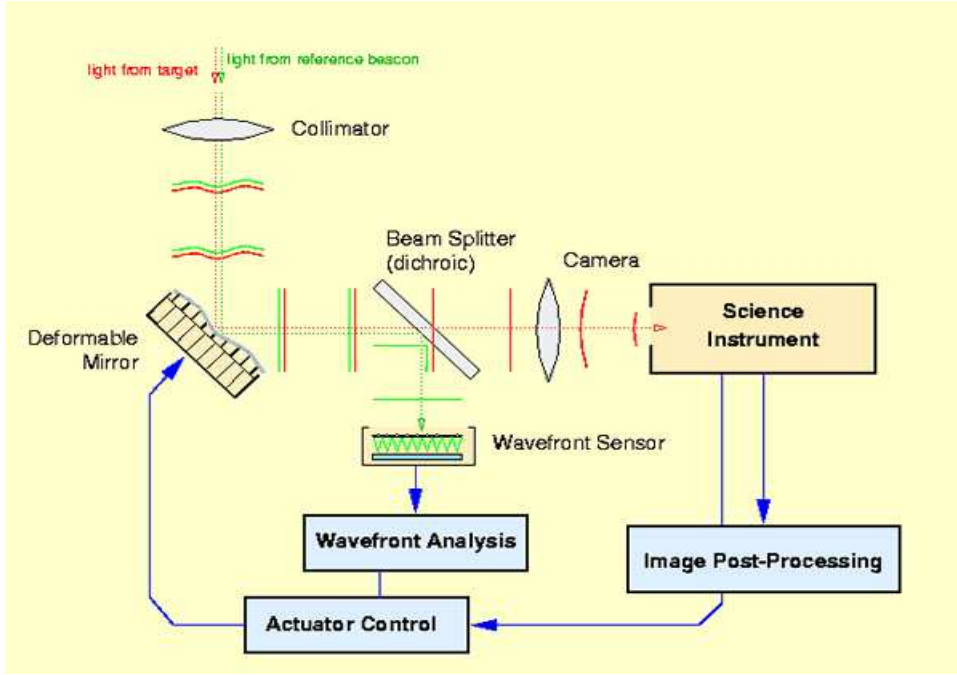


Figure 2. Schematic diagram of a simple adaptive optics system.

aperture plane, while u, v have units of inverse distance and represent scaled location in the image plane, which corresponds to angular position on the sky.

The term ϕ in the exponential in Eq. (2.11) represents the wavefront aberrations, and is often called the *phase*. To illustrate, consider the planar *tip-tilt aberration*,

$$\phi_{\theta}(x, y) = 2\pi(\theta_1 x + \theta_2 y), \quad (2.12)$$

where $\theta = (\theta_1, \theta_2)$ is fixed. Substituting (2.12) into (2.11), we see that

$$\begin{aligned} s_{\phi_{\theta}}(u, v) &= \left| \int \int A(u, v) e^{-i2\pi[x(u-\theta_1)+y(v-\theta_2)]} dx dy \right|^2 \\ &= s_0(u - \theta_1, v - \theta_2), \end{aligned} \quad (2.13)$$

where

$$s_0(u, v) = |\mathcal{F}\{A\}(u, v)|^2 = \left| \int \int A(x, y) e^{i2\pi(xu+yv)} dx dy \right|^2 \quad (2.14)$$

is the *diffraction limited PSF*. For a telescope with a circular aperture, this is the square of an Airy function, which comes to resemble a delta function as the aperture diameter increases [29]. From (2.13), (2.14), and (2.11), we see that the effect of a tip-tilt wavefront aberration is to induce a linear shift, or translation, in the image.

A common measure of image quality is the *Strehl ratio*,

$$s_{\phi}(0, 0)/s_0(0, 0). \quad (2.15)$$

Note that the denominator is the peak value of the diffraction limited PSF, while the numerator is the aberrated PSF, evaluated at the origin. From Eq. (2.14),

$$s_0(0, 0) = \left| \int \int A(x, y) dx dy \right|^2. \quad (2.16)$$

Similarly,

$$s_\phi(0,0) = \left| \int \int A(x,y) e^{i\phi(x,y)} dx dy \right|^2. \quad (2.17)$$

We may assume that

$$\int \int A(x,y) \phi(x,y) dx dy = 0. \quad (2.18)$$

Otherwise, we multiply the integral in (2.17) by e^{-ic} , where c is the nonzero value on the LHS in (2.18)). The physical interpretation is that adding an arbitrary constant shift, or “piston mode”, to the phase has no effect on the PSF.

If the phase ϕ is relatively small, we may expand the exponential about $\phi = 0$ to second order to obtain the Strehl ratio approximation

$$\frac{s_\phi(0,0)}{s_0(0,0)} = 1 - \frac{\int \int A \phi^2 dx dy}{\int \int A dx dy} + \mathcal{O} \left\{ \left(\int \int A \phi^2 dx dy \right)^2 \right\}. \quad (2.19)$$

Consequently, large Strehl ratios (and good image quality) can be attained by minimizing the mean squared phase over the telescope aperture.

The following subsection explores the relationship between wavefront aberrations and variations in the refractive index of the atmosphere.

2.2. Atmospheric Light Propagation Model

We model electromagnetic wave propagation through the atmosphere with the Helmholtz equation,

$$\nabla^2 U + k^2(\mathbf{x}) U = 0. \quad (2.20)$$

Here U is the time-harmonic scalar electric field, $k(\mathbf{x}) = k_0 n(\mathbf{x})$, where n is the refractive index, and the frequency

$$k_0 = 2\pi/\lambda, \quad (2.21)$$

where λ denotes the wavelength of the light. Because the atmosphere is weakly scattering at visible wavelengths,

$$k(\mathbf{x}) = k_0(1 + \delta n(\mathbf{x})), \quad (2.22)$$

where the refractive index perturbation δn and its gradient are small. To first order in δn , the Rytov approximation [55] yields

$$U(\mathbf{x}) = U_0(\mathbf{x}) e^{\Phi(\mathbf{x})}. \quad (2.23)$$

Here $U_0(\mathbf{x})$ is a particular solution to the constant coefficient Helmholtz equation (2.20) with $k(\mathbf{x}) = k_0$ which satisfies prescribed boundary conditions, and

$$\Phi(\mathbf{x}) = -\frac{2k_0^2}{U_0(\mathbf{x})} \int \int \int G(\mathbf{x} - \mathbf{x}') U_0(\mathbf{x}') \delta n(\mathbf{x}') d\mathbf{x}', \quad (2.24)$$

where the free-space Green's function

$$G(\mathbf{x}) = -\frac{e^{ik_0|\mathbf{x}|}}{4\pi|\mathbf{x}|}.$$

In the context of astronomical imaging, the region of integration in Eq. (2.24) is an infinite slab of thickness H , the height of the atmosphere. To model a distant

bright star we take a point source at infinity, which gives rise to a plane-wave particular solution

$$U_0(\mathbf{x}) = e^{-ik_0(\mathbf{x} \cdot \boldsymbol{\theta})}, \quad (2.25)$$

where $\boldsymbol{\theta} = (\theta_1, \theta_2, \theta_3)$ is a unit vector which specifies the direction of the star. Denoting $\mathbf{x}' = (\xi, \eta, \zeta)$, placing the telescope aperture in the xy-plane, so the slab integration region in Eq. (2.24) has vertical extent $0 \leq \zeta \leq H$, taking $\mathbf{x} = (x, y, 0)$ to be a point inside the aperture, and substituting (2.25), we obtain from (2.24)

$$\Phi(x, y, 0) = 2k_0^2 e^{ik_0(x\theta_1 + y\theta_2)} \int_0^H \left[\int_{-\infty}^{\infty} \int_{-\infty}^{\infty} f e^{ik_0 g} d\xi d\eta \right] d\zeta, \quad (2.26)$$

where

$$f = \delta n(\xi, \eta, \zeta) / 4\pi R(\xi, \eta, \zeta; x, y) \quad (2.27)$$

and

$$g = R(\xi, \eta, \zeta; x, y) - \theta_1 \xi - \theta_2 \eta - \theta_3 \zeta \quad (2.28)$$

with

$$R(\xi, \eta, \zeta; x, y) = \sqrt{(\xi - x)^2 + (\eta - y)^2 + \zeta^2}. \quad (2.29)$$

We apply to the bracketed term in (2.26) the 2-d stationary phase formula,

$$\int_{-\infty}^{\infty} \int_{-\infty}^{\infty} f(\xi, \eta) e^{ik_0 g(\xi, \eta)} d\xi d\eta \sim \frac{i2\pi}{k_0} \frac{f(\bar{\xi}, \bar{\eta}) e^{ik_0 g(\bar{\xi}, \bar{\eta})}}{\sqrt{\frac{\partial^2 g}{\partial \xi^2}(\bar{\xi}, \bar{\eta}) \frac{\partial^2 g}{\partial \eta^2}(\bar{\xi}, \bar{\eta})}}, \quad (2.30)$$

where \sim means “asymptotically equal to as $k_0 \rightarrow \infty$ ” and $(\bar{\xi}, \bar{\eta})$ is the stationary point, at which the gradient of g vanishes. For any $\zeta > 0$, g is strictly convex so the stationary point is unique. Note that

$$\frac{\partial g}{\partial \xi} = (\xi - x)/R - \theta_1, \quad \frac{\partial g}{\partial \eta} = (\eta - y)/R - \theta_2. \quad (2.31)$$

We assume that $\boldsymbol{\theta}$ points nearly in the direction of the optical axis of the telescope (the z axis), so $\theta_3 \approx 1 \gg \theta_1, \theta_2$. Then

$$\bar{\xi} \approx x + \theta_1 \zeta, \quad \bar{\eta} \approx y + \theta_2 \zeta, \quad (2.32)$$

and

$$R(\bar{\xi}, \bar{\eta}, \zeta; x, y) \approx \zeta \sqrt{\theta_1^2 + \theta_2^2 + 1} \approx \zeta. \quad (2.33)$$

Consequently,

$$\Phi(x, y, 0) \sim ik_0 \int_0^H \delta n(x + \theta_1 \zeta, y + \theta_2 \zeta, \zeta) d\zeta \quad (2.34)$$

as $k_0 \rightarrow \infty$ and as $\boldsymbol{\theta} \rightarrow (0, 0, 1)$.

Note that the integral term is simply a line integral along ray paths for the plane-wave incident field (2.25). We will use the notation $\phi(x, y; \boldsymbol{\theta})$ to represent the right-hand-side of Eq. (2.34) without the term ik_0 , and we will refer to it as the *aperture-plane phase aberration* at location (x, y) in the direction $\boldsymbol{\theta}$.

We next discuss turbulence, which is the primary source of phase aberrations in atmospheric optics.

2.3. Turbulence Model

Atmospheric turbulence is the highly irregular mixing of warm and cold air, driven by the sun's heat and by wind. The phase aberration ϕ resulting from light propagation through a given layer in the turbulent atmosphere can be accurately modeled as a realization of a strictly stationary Gaussian stochastic process with von Karman statistics [54]. Such a process has zero mean and is characterized by its covariance, which depends only on spatial separation $\Delta \mathbf{x}$,

$$C_\phi(\Delta \mathbf{x}) = \langle \phi(x + \Delta x, y + \Delta y) \phi(x, y) \rangle. \quad (2.35)$$

The *power spectral density* is the Fourier transform of the covariance, and is given in the von Karman case by

$$\hat{C}_\phi(\boldsymbol{\kappa}) = c_0(|\boldsymbol{\kappa}|^2 + 1/L_0^2)^{-11/6}. \quad (2.36)$$

Here L_0 represents the outer scale of the turbulence and c_0 quantifies the turbulence strength. It is customary in AO to denote the spatial frequency of turbulence by $\boldsymbol{\kappa} = (\kappa_x, \kappa_y)$. One can interpret the right-hand-side of Eq. (2.36) as the amount turbulent energy concentrated at a particular spatial frequency. As $L_0 \rightarrow \infty$, one obtains Kolmogorov turbulence, with its characteristic $-11/3$ rate of decay with increasing spatial frequency.

2.4. Deformable Mirror Model

A *deformable mirror* (DM) consists of a thin, flexible facesheet coated with highly reflective material. Actuators attached to the back of the facesheet displace the facesheet in a controllable manner. Arguably the most important DM technologies for astronomical AO are (i) piezo-stack DMs, which use stacks of piezo-ceramic disks for actuation; (ii) adaptive secondary mirrors; and (iii) Micro Electro Mechanical System (MEMS) devices. Adaptive secondary mirrors consist of a thin curved facesheet controlled by voice coil actuators, whose positions are measured and controlled using local position sensors referenced to a stable support structure. MEMS consist of tiny actuators, sensors, and electronics, all integrated together on a common silicon substrate using micro fabrication technology. We present here a relatively simple model for DM facesheet displacement based on static thin plate theory [60].

When the DM is in static equilibrium, forces due to the actuators acting on the facesheet are balanced by restoring forces due to flexure of the facesheet. If the actuator contact points are relatively small, the facesheet is composed of an elastic material like glass of uniform thickness, and the local curvature of the facesheet is small relative to the thickness, we may ignore longitudinal displacements to obtain

$$D_{\text{fs}} \nabla^4 w + \sum_{i=1}^{n_a} p_i \delta(\mathbf{x} - \mathbf{x}_i) = 0. \quad (2.37)$$

Here $w(\mathbf{x})$ denotes transverse displacement, or deflection, of the facesheet at longitudinal position $\mathbf{x} = (x, y)$; D_{fs} denotes flexural rigidity of the facesheet; p_i denotes the point load on the facesheet due to i th actuator; \mathbf{x}_i denotes actuator location; $\delta(\cdot)$ denotes the Dirac Delta; n_a denotes number of actuators; and ∇^4 denotes the 2-d biharmonic, or squared Laplacian, operator.

For each of the actuators, we employ an algebraic model,

$$z_i = r(p_i, V_i), \quad i = 1, \dots, n_a, \quad (2.38)$$

where z_i denotes vertical deflection of i th actuator; p_i again denotes the load on facesheet due to i th actuator; and V_i denotes the “command voltage” applied to i th actuator. If the actuators are firmly attached to facesheet, we obtain the coupling condition

$$w(\mathbf{x}_i) = z_i, \quad i = 1, \dots, n_a. \quad (2.39)$$

DM deflection is typically measured relative to a constant “bias” deflection, obtained when a bias voltage \bar{V} is applied simultaneously to all the actuators. If the DM facesheet is not supported at the edges, one may assume free boundary conditions. At constant bias deflection, the biharmonic term in (2.37) vanishes and there is no contribution from the boundaries. Hence the point load $p_i = 0$ for each i . We may assume with loss of generality that the bias deflection is zero. From (2.37)-(2.39), we obtain

$$0 = r(0, \bar{V}). \quad (2.40)$$

Now suppose we apply to each actuator a voltage V_i for which $\Delta V_i = V_i - \bar{V}$ and the corresponding deflection $w(\mathbf{x}_i) = z_i$ and load p_i are small. Taylor’s Theorem then yields

$$w(x_i) = r_p(0, \bar{V}) p_i + r_V(0, \bar{V}) \Delta V_i + \mathcal{O}(p_i^2) + \mathcal{O}((\Delta V_i)^2), \quad (2.41)$$

where r_p, r_V denote partial derivatives with respect to p and V , respectively. Dropping the error terms, solving for p_i , and substituting in (2.37), we obtain the 2-parameter model

$$\nabla^4 w + \beta_1 \sum_{i=1}^{n_a} w(\mathbf{x}_i) \delta(\mathbf{x} - \mathbf{x}_i) = \beta_2 \sum_{i=1}^{n_a} \Delta V_i \delta(\mathbf{x} - \mathbf{x}_i), \quad (2.42)$$

where

$$\beta_1 = \frac{1}{D_{fs} r_p(0, \bar{V})}, \quad \beta_2 = \frac{r_V(0, \bar{V})}{D_{fs} r_p(0, \bar{V})} = r_V(0, \bar{V}) \beta_1. \quad (2.43)$$

The DM actuators are typically laid out on a regular rectangular grid. By “poking”, or applying non-bias voltage to a single interior actuator, and then measuring the resulting facesheet deflection, one obtains the (interior) actuator influence function for the DM. The plots in Fig. 3 show a measured influence function, together with a fit obtained by solving Eq. (2.42) for a particular choice of β_1, β_2 .

In section 5 we will discuss the estimation of model parameters like β_1 and β_2 . We will also discuss more general parameter identification problems that occur, for example, when the linear approximation to the actuator model equation (2.38) lacks sufficient accuracy.

2.5. Wavefront fitting

We next apply our simple DM model to the correction of wavefront aberrations. We can express (2.42) as a linear operator equation

$$Aw = F\mathbf{a}. \quad (2.44)$$

Here \mathbf{a} denotes the vector of differential command voltages ΔV_i , $i = 1, \dots, n_a$. Assuming the operator A is invertible, we obtain

$$w = H\mathbf{a} \quad \text{where} \quad H = A^{-1}F. \quad (2.45)$$

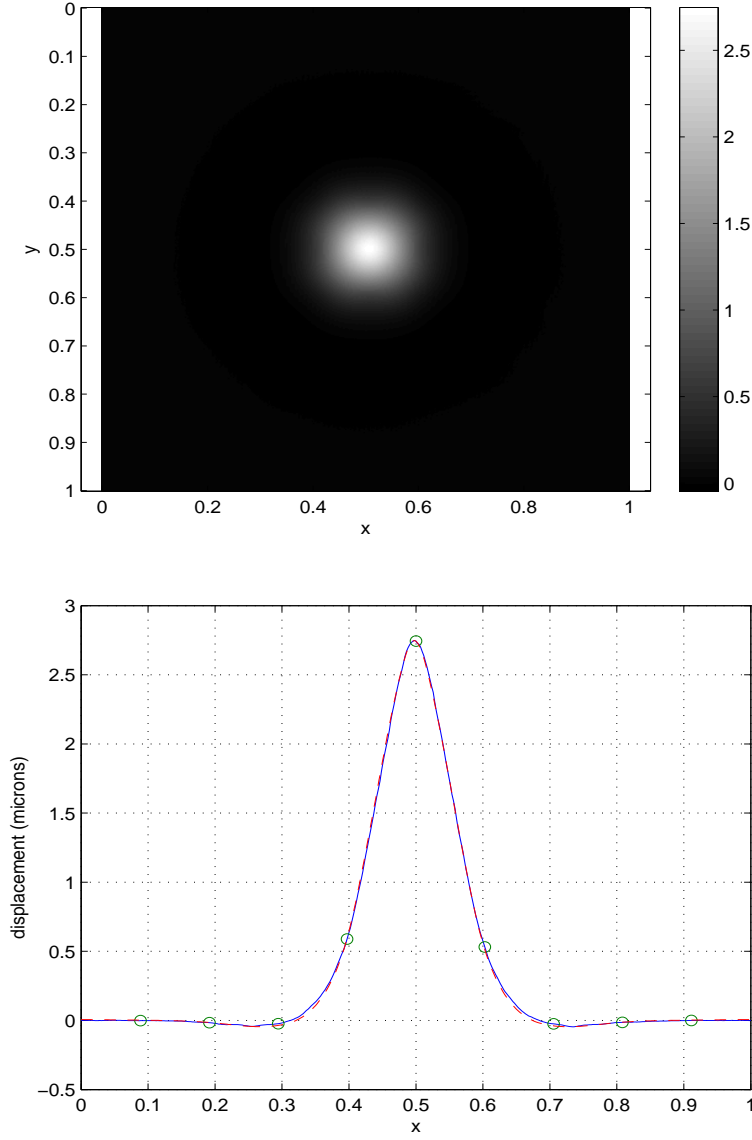


Figure 3. Deformable mirror influence function. Intensity plot at top shows facesheet deflection $w(x, y)$ in microns resulting from a single poked actuator at normalized location $(0.5, 0.5)$. Solid blue curve in the bottom plot shows x-cross section $w(x, 0.5)$, $0 \leq x \leq 1$, with actuator locations marked by circles. The red dashed curve represents a fit based on the linearized model (2.42).

Given a particular phase ϕ , our goal is to select actuator commands \mathbf{a} so that the mirror deflection w nearly matches the phase. This motivates the minimization of the least squares functional

$$J(\mathbf{a}) = \|\mathbf{H}\mathbf{a} - \phi\|^2,$$

whose minimizer is given by $\mathbf{a}_{LS} = H^\dagger \phi$. If the operator H has a trivial null space, then the pseudo-inverse has the representation

$$H^\dagger = (H^T H)^{-1} H^T. \quad (2.46)$$

2.6. Wavefront Sensor Model

In practice, the wavefront aberration ϕ is not known a priori and must be estimated from output of a wavefront sensor. One of the most commonly used devices to measure wavefront aberrations is the Shack-Hartmann wavefront sensor; see Fig. 4. This device consists of an array of lenslets, distributed on a rectangular array across the field of view of the sensor. Light falling on a particular lenslet is focused on a photodetector behind the lenslet. From discussion in Section 2.1, a tip-tilt wavefront aberration gave rise to a shift in the image. Hence, if the wavefront of the incoming light is locally planar, the lenslet focuses light to a spot whose x- and y-components of location on the photodetector are proportional to the x- and y-components of the slope of the wavefront. A simple model for the x-component of the sensor readout is then

$$s_{i,j}^x = c \int \int_{\Omega_{i,j}} \frac{\partial \phi}{\partial x} dx dy + \eta_{i,j}, \quad (2.47)$$

where c is a known proportionality constant, and similarly for the y-component. Here $\Omega_{i,j}$ denotes the field of view of ijth lenslet in the rectangular array, and $\eta_{i,j}$ represents sensor noise. The $\eta_{i,j}$ are typically modeled as independent random variables with zero means.

A centroid scheme is typically used to measure the shifts that give rise to local wavefront slope estimates. Beneath each lenslet in a Shack-Hartmann sensor lies a photodetector array. Assume a 2-by-2 array which produces voltage responses to intensity labeled I_1, I_2, I_3 , and I_4 as we move clockwise from the upper left entry of the array. The vertical and horizontal components of the shift are taken to be proportional to $(I_1 + I_2 - I_3 - I_4)/(I_1 + I_2 + I_3 + I_4)$ and $(I_1 - I_2 - I_3 + I_4)/(I_1 + I_2 + I_3 + I_4)$, respectively. More sophisticated matched filtering techniques for wavefront sensing will be presented in Section 3.3.1.

2.7. Linear Minimum Variance Wavefront Reconstruction

From the previous discussion of Strehl, to improve image quality it suffices to minimize the mean squared phase; see Eq. (2.19). To this end, we model the phase from an optical system with simple single conjugate AO correction as

$$\phi_{\text{resid}}(\mathbf{x}) = \phi_{\text{DM}}(\mathbf{x}) - \phi_{\text{atmos}}(\mathbf{x}), \quad \mathbf{x} \in \Omega, \quad (2.48)$$

where ϕ_{atmos} represents the wavefront aberrations in the aperture Ω due to atmospheric turbulence, and ϕ_{DM} denotes AO correction obtained from the deformable mirror. Motivated by Eq. (2.45), we assume a linear relationship,

$$\phi_{\text{DM}} = H \mathbf{a} \quad (2.49)$$

between the AO correction and the actuator command vector \mathbf{a} . Our goal is to pick \mathbf{a} to minimize the mean squared residual wavefront error,

$$J = \langle ||H_{\text{DM}} \mathbf{a} - \phi_{\text{atmos}}||_{L^2(\Omega)}^2 \rangle, \quad (2.50)$$

given a linear dependence of \mathbf{a} on the vector \mathbf{s} of sensor measurements,

$$\mathbf{a} = R \mathbf{s}. \quad (2.51)$$

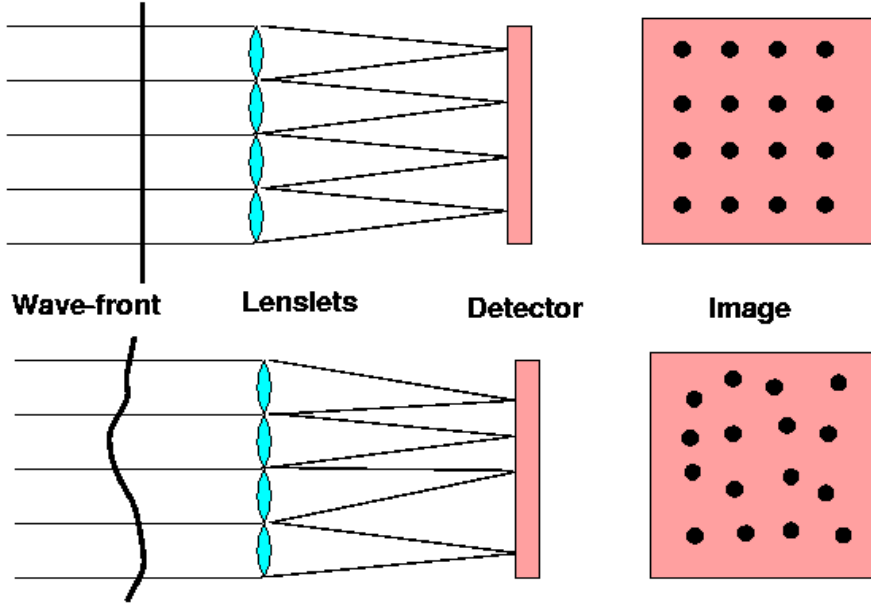


Figure 4. Schematic diagram of a Shack-Hartmann wavefront sensor. To first order, displacement of an image spot is proportional to the local gradient of the wavefront.

Motivated by section 2.6, we assume a linear, additive, zero mean noise model,

$$\mathbf{s} = G\phi_{\text{atmos}} + \boldsymbol{\eta}, \quad (2.52)$$

relating the sensor measurements \mathbf{s} to the atmospheric phase aberrations; see Eq. (2.47). This “open loop” model suggests that the sensors appear “upstream” from the corrective elements. Due to dynamic range considerations, practical AO systems operate in “closed loop”, in which case ϕ_{atmos} in Eq. (2.48) is replaced by ϕ_{resid} . By “closed loop” we mean that the sensors appear downstream from the DM correction, as is shown in Fig. 2. A so-called “pseudo-open loop” scheme has been proposed to allow one to deal with closed loop sensor data in an open loop framework. See section 4.2 for details.

Substituting (2.52) and (2.51) into (2.50), we obtain

$$\begin{aligned} J(R) &= \langle ||(HRG - I)\phi_{\text{atmos}} + HR\boldsymbol{\eta}||^2 \rangle \\ &= \text{trace}\{(HRG - I)C_\phi(HRG - I)^T + (HR)C_\eta(HR)^T\}, \\ &= \text{trace}\{HRAR^T H^T - HRB - B^T R^T H^T\}, \end{aligned} \quad (2.53)$$

where C_ϕ and C_η are the covariances for the atmospheric phase ϕ_{atmos} and the sensor noise $\boldsymbol{\eta}$, respectively, and

$$A = GC_\phi G^T + C_\eta, \quad B = GC_\phi. \quad (2.54)$$

We next compute the directional derivative of J and set it equal to zero to obtain a minimizer. For any matrix S of appropriate size,

$$\frac{J(R + \tau S) - J(R)}{\tau} = 2 \sum_i [HRAS^T H^T - B^T S^T H^T]_{ii} + \mathcal{O}(\tau)$$

Taking S_{jk} to have a 1 in entry j, k and zeros elsewhere, and taking the limit as $\tau \rightarrow 0$, we obtain the directional derivative

$$\begin{aligned} \frac{1}{2}DJ(R; S_{jk}) &= \sum_i [HRA]_{ij} [H^T]_{ki} - \sum_i [B^T]_{ij} [H^T]_{ki} \\ &= [H^T(HRA - B^T)]_{kj}. \end{aligned}$$

At a minimizer $R = R_{\text{MV}}$ for J , the above quantity must vanish for any index pair j, k , so we obtain the following representation for the minimum variance reconstructor,

$$\begin{aligned} R_{\text{MV}} &= (H^T H)^{-1} H^T B^T A^{-1} \\ &= (H^T H)^{-1} H^T G^T (G C_\phi G^T + C_\eta)^{-1} \\ &= (H^T H)^{-1} H^T (G^T C_\eta^{-1} G + C_\phi^{-1})^{-1} G^T C_\eta^{-1}. \end{aligned} \quad (2.55)$$

Comparing (2.55) with (2.46), we see that

$$R_{\text{MV}} \mathbf{s} = H^\dagger \phi_{\text{MV}}, \quad (2.56)$$

where

$$\phi_{\text{MV}} = (G^T C_\eta^{-1} G + C_\phi^{-1})^{-1} G^T C_\eta^{-1} \mathbf{s}. \quad (2.57)$$

This is the *maximum a posteriori* (MAP) estimate of the atmospheric phase ϕ_{atmos} from sensor measurements \mathbf{s} , provided the stationary stochastic process ϕ_{atmos} has zero mean and Gaussian statistics, and \mathbf{s} is a Gaussian random vector with zero mean.

ϕ_{MV} also minimizes the Tikhonov functional

$$T(\phi) = \|G\phi - \mathbf{s}\|_{C_\eta^{-1}}^2 + \|\phi\|_{C_\phi^{-1}}^2, \quad (2.58)$$

where $\|\cdot\|_A$ denotes the A -weighted norm. In the discrete (vector) case this takes the form

$$\|\mathbf{f}\|_A^2 = \sqrt{\sum_i \sum_j A_{ij} f_i f_j},$$

where A is a symmetric positive definite matrix. In the continuous (function) case,

$$\|f\|_A^2 = \sqrt{\int \int A(\mathbf{x}, \mathbf{x}') f(\mathbf{x}) f(\mathbf{x}') d\mathbf{x} d\mathbf{x}'},$$

where A is positive, self-adjoint linear operator. Given the von Karman turbulence model from section 2.3, the inverse phase covariance in (2.58) is a pseudo-differential operator of order 11/3. Hence this inverse covariance can be viewed as a regularization operator.

Note that we have decomposed the wavefront estimation process into two steps: (i) the statistical estimation of the atmospheric phase ϕ_{atmos} from sensor measurements s related by the model (2.52); and (ii) the selection of the commands \mathbf{a}_{MV} to fit the DM deflection to the estimated phase ϕ_{MV} in a least squares sense. This two-step decomposition of the reconstruction process is a special case of the separation principle of stochastic control [7]. In Section 4, we apply an analogous two-step process to a more complex Multi-Conjugate Adaptive Optics system.

2.7.1. Least-squares wavefront reconstruction. It should also be noted that conventional AO systems do not rely on minimum variance wavefront reconstructors. They instead make use of least-squares reconstructors [32], where the actuator commands \mathbf{a} are chosen to minimize

$$J_{\text{LS}}(\mathbf{a}) = \|GH\mathbf{a} - \mathbf{s}\|_{C_\eta^{-1}}^2. \quad (2.59)$$

In this context the operator $D = GH$, which is often called the *poke matrix* for the AO system, can be viewed as a discrete gradient operator. Any minimizer of J_{LS} must satisfy

$$(D^T C_\eta^{-1} D)\mathbf{a} = D^T C_\eta^{-1} \mathbf{s}, \quad (2.60)$$

a system that can be viewed as a discrete Poisson equation. Poisson equations that typically arise in applied mathematics are well-posed, so no regularization is needed. In conventional AO the situation is somewhat more complicated. The constant vectors lie in the null space of the discrete gradient D , and in the null space of the discrete Laplacian $D^T C_\eta^{-1} D$. These can be filtered out and have no effect on image formation; replacing ϕ by $\phi + c$ does not change the point spread function in Eq. (2.11) when the constant c is real-valued. There are some additional null vectors, often called “waffle modes” [43], that arise in least squares wavefront reconstruction, but these are of low dimension and can also be easily filtered out.

In section 4 we will investigate more complex AO systems for which the wavefront reconstruction problem is highly ill-posed. In this case regularization is essential.

2.8. AO vs image post-processing

Given a basic understanding of AO, the reader should now be able address the following question: Why bother doing AO when one could simply form an image and then enhance it using, for example, deconvolution techniques? It is extremely difficult to form diffraction limited images of certain astronomical objects without AO. Image deconvolution is an ill-posed process and requires regularization. This entails a trade-off between goodness of fit to the data and stability to reduce noise amplification. Relatively dim astronomical objects yield images with relatively low signal-to-noise ratios. In order to prevent noise amplification, the regularization has the effect of filtering out certain components of the reconstructed image; see [63] for an analysis. This leads to a loss of information that can only be retrieved with very strong a priori information about the true image.

Signal-to-noise ratios can be increased by temporal averaging. However, the PSF arising from the averaging process is much broader than that of the nearly instantaneous PSF; see [54]. This means that the resulting deconvolution problem is much more ill-posed. In effect, no gain can be achieved from this type of averaging. To be more precise, the long-exposure PSF arising from uncompensated atmospheric turbulence can be well approximated by a Gaussian whose width σ increases with exposure time. The (compact) integral operator whose kernel is this Gaussian has singular values which decay as $\exp(-\sigma^2(u^2 + v^2))$, where (u, v) denotes 2-dimensional spatial frequency. Deconvolution requires the inversion of this operator, and some sort of filtering is needed to negate the effects of tiny singular values. Unless σ is quite small (the exposure time is relatively short), only a few singular components can be retained and a high-resolution reconstruction is impossible.

Another alternative is to solve a sequence of deconvolution problems with the instantaneous PSF and then average the resulting reconstructed images. The

disadvantage of this approach is that it requires precise knowledge of the (non-Gaussian) instantaneous PSF and it requires an enormous amount of computational processing to achieve a high-resolution image. It is much cheaper to apply physical compensation to the light, in the form of AO wavefront correction, before the image is formed. One can then average AO-corrected images by simply keeping the telescope focused on a single spot on the sky and collecting photons with a recording device like a CCD array.

It should be noted that a large fraction of the observing time in astronomy is devoted to spectroscopy as opposed to imaging. Image post-processing serves no useful purpose for the spectroscopy of unresolved sources, such as stars. For this application, the purpose of adaptive optics is to concentrate the light to pass through a narrower spectrometer slit, which enables higher spectral resolution and reduces the measurement noise due to the sky background. For both of these parameters, the performance improvement obtained through the use of AO is roughly proportional to the reduction in the image diameter.

We next present selected research topics in astronomical AO.

3. Laser Guide Star Adaptive Optics

For astronomical adaptive optics, the most straightforward light source to use for wavefront sensing is simply a star. Unfortunately, the number of stars which are sufficiently bright to use for this purpose is fairly limited. Additionally, the field-of-view over which turbulence-induced wavefront errors are correlated is limited by the effect of turbulence at nonzero altitude, as is illustrated in Fig. 5a. As a consequence only a small percentage of possible science objects may be observed using “natural guide star” (NGS) AO. An alternative wavefront sensing light source is required for the remainder of the sky.

To overcome this limitation, astronomers and other observers are now generating artificial guide stars by projecting laser beams into the sky and observing the return signal generated by atmospheric backscatter from ranges from 10 to 90 km [40]. Although the basic principles of adaptive optics described above remain applicable to such “laser guide star” LGS AO systems, a variety of new issues arise due to (i) the finite range of the light source, (ii) the somewhat uncertain position of the light source, and (iii) the nonzero physical extent of the light source. The analytical and practical consequences of these issues are outlined in the following paragraphs.

3.1. Finite Range Source Effects

The finite range of the LGS is the most fundamental distinction from the natural guide star case. Because it is possible to “range gate” the backscattered laser light, to first order the LGS may be approximated at a point light source located at coordinates $\mathbf{x}_0 = (x_0, y_0, z_0)$ relative to the telescope aperture plane. The wavefront propagating from this source is now spherical instead of effectively planar, and the particular solution for the turbulence-free case becomes

$$U_0(\mathbf{x}) = e^{-k_0|\mathbf{x}-\mathbf{x}_0|}. \quad (3.1)$$

Proceeding as above, Eq. (2.34) for the phase distortion introduced by atmospheric turbulence remains valid, except that the ray angle (θ_1, θ_2) now depends upon the point \mathbf{x} according to the formula

$$\theta_1(x) = (x_0 - x)/z_0 \quad \text{and} \quad \theta_2(y) = (y_0 - y)/z_0. \quad (3.2)$$

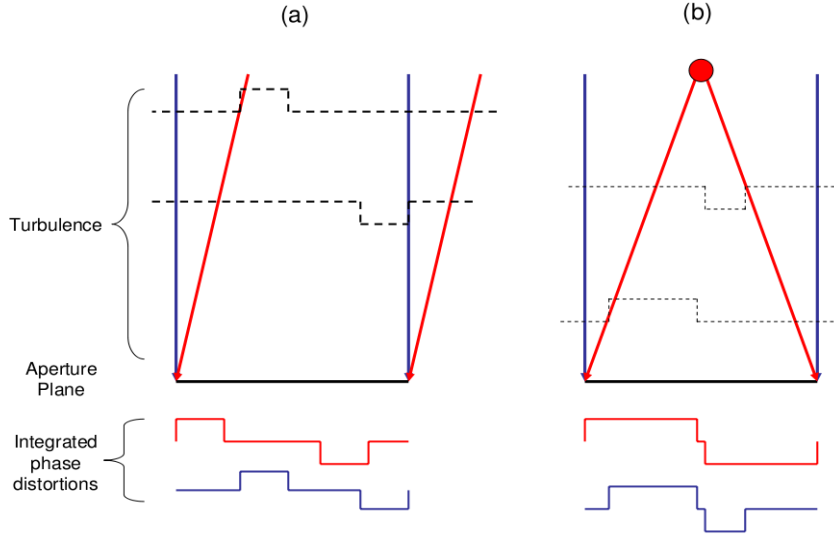


Figure 5. Wavefront sensing geometry with (a) an off-axis natural guide star or (b) an artificially generated laser guide star at finite range.

This geometry is illustrated in Fig. 5b. As might be expected, the ray paths to all points within the aperture diverge from the location of the finite-range LGS.

This divergent ray geometry is frequently referred to as the LGS “cone effect.” As illustrated in Fig. 5b, light from the LGS does not sample atmospheric turbulence along the parallel ray paths associated with a science object at infinity. As a result, it is not possible to precisely measure and correct for the impact of atmospheric turbulence upon a science observation using only a single LGS, and the magnitude of the measurement error increases with increasing aperture diameter. This limitation motivates the interest in multi-guidestar systems and atmospheric tomography, as described in Section 4 below.

3.2. Source Position Uncertainty Effects

A second limitation of LGS wavefront sensing is the uncertain location of the source. The pointing of the laser beacon on the sky cannot be controlled precisely, since the laser and its associated projection optics are not perfectly stable and the outgoing laser beam is further deflected by turbulence as it propagates upward. If the overall pointing of the laser beam is in error by an angle (θ_x, θ_y) , the particular solution to the turbulence-free case becomes

$$\begin{aligned}
 U_0(\mathbf{x}_0) &= e^{-ik_0[(x-x_0-\theta_x z_0)^2 + (y-y_0-\theta_y z_0)^2 + z_0^2]^{1/2}} \\
 &\approx e^{-ik_0|\mathbf{x}-\mathbf{x}_0|} e^{ik_0[\theta_x(x-x_0) + \theta_y(y-y_0)]}.
 \end{aligned} \tag{3.3}$$

The first-order impact of this pointing error is to introduce an uncertain tip-tilt component in the measured wavefront. The error is generally too large to be ignored

(in fact, a majority of the wavefront error introduced by atmospheric turbulence is contained in the two tip and tilt modes), and an auxiliary natural guide star must still be employed to measure tip/tilt. This requirement constrains the “sky coverage” achievable using LGS adaptive optics, but the restriction is less severe than for NGS AO because the natural star need only be sufficiently bright to measure two wavefront modes instead of many.

As a further consequence, the wavefront reconstruction operator for an LGS AO system must operate on a combination of LGS and NGS wavefront measurements. The MAP formulation described above remains valid, but the measurement equation and the associated measurement noise statistics must be modified. If the cone effect is neglected (as it is in all operational LGS AO systems), the wavefront measurement equation now becomes

$$s = \begin{pmatrix} s_{\text{LGS}} \\ s_{\text{NGS}} \end{pmatrix} = \begin{pmatrix} G_{\text{LGS}} \\ G_{\text{NGS}} \end{pmatrix} \phi_{\text{atmos}} + \begin{pmatrix} \eta_{\text{LGS}} \\ \eta_{\text{NGS}} \end{pmatrix}. \quad (3.4)$$

Here s_{NGS} is a 2-vector describing the position of the natural star observed through an NGS wavefront sensor with only a single subaperture equal to the full telescope aperture. To model the effect of LGS pointing uncertainty, the measurement noise covariance matrix takes the form

$$C_\eta = \begin{pmatrix} C_{\eta,\text{LGS}} + \sigma_\theta^2 T^T T & 0 \\ 0 & C_{\eta,\text{NGS}} \end{pmatrix}. \quad (3.5)$$

Here $C_{\eta,\text{LGS}}$ and $C_{\eta,\text{NGS}}$ describe the measurement noise due to the LGS and NGS wavefront sensors themselves, σ_θ^2 is the mean-square laser pointing error, and T is a 2-column matrix consisting of the measurement modes which are corrupted by the pointing errors:

$$T_{ij} = \begin{cases} 1 & \text{if } j = 1 \text{ and } s_{\text{LGS},i} \text{ is an } x\text{-gradient measurement;} \\ 1 & \text{if } j = 2 \text{ and } s_{\text{LGS},i} \text{ is an } y\text{-gradient measurement;} \\ 0 & \text{otherwise.} \end{cases} \quad (3.6)$$

This representation may be simplified by allowing the tip/tilt variance σ_θ^2 to approach infinity. In this case, the tip/tilt modes of the LGS WFS measurement are nulled via a projection onto the orthogonal complement of the 2-dimensional subspace spanned by the columns of T , and these modes are effectively determined by the value of the NGS WFS measurements.

3.3. Extended Source Effects

A third implementation issue is introduced by the fact that the laser guide star is *not* an ideal point source, but is instead an extended, 3-dimensional source $O(x, y, z)$. Each subaperture in the wavefront sensor views this object along a separate line-of-sight and consequently forms a different two-dimensional image. The geometry of this process is illustrated in Fig. 6. A laser beam projected from coordinates $(0, 0, 0)$ is pointed and focussed at a nominal guide star location (x_0, y_0, z_0) , which is imaged through a WFS subaperture centered at coordinates $(x_s, y_s, 0)$. The nominal image I_0 of the extended guidestar O is then given by

$$I_0(\theta_x, \theta_y) \approx \int_{H_1}^{H_2} \left(\frac{A}{z^2} \right) \int \int O(x, y, z) \times \text{PSF} \left(\theta_x - \frac{x - x(z)}{z}, \theta_y - \frac{y - y(z)}{z} \right) dx dy dz. \quad (3.7)$$

Here H_1 and H_2 are the lower and upper bounds of the source O , A is the area of the subaperture, PSF is the subaperture point spread function for objects located near the nominal LGS location (x_0, y_0, z_0) , and $x(z)$ lies on the subaperture line-of-sight at range z according to the formula

$$x(z) = x_0 + \left(\frac{z - z_0}{z_0} \right) (x_0 - x_s), \quad (3.8)$$

and similarly for $y(z)$.

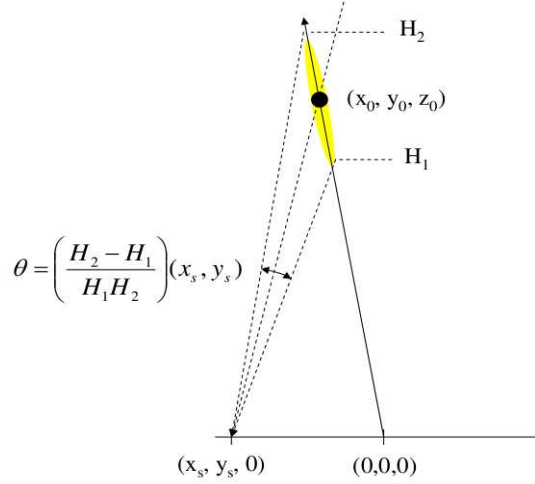


Figure 6. Imaging geometry for extended laser guide stars.

The LGS image in each subaperture is elongated because the object O is approximately a long, narrow cylinder oriented along the direction of laser propagation. At the range $z = Z$, most of the energy in $O(x, y, Z)$ is concentrated around the point with coordinates $(x, y) = (z/z_0)(x_0, y_0)$, which images onto the point $(\theta_x, \theta_y) = (z_0^{-1} - Z^{-1})(x_s, y_s)$. As Z varies from H_1 to H_2 , this point sweeps out an elongated image of length and orientation $\left(\frac{H_2 - H_1}{H_2 H_1} \right) (x_s, y_s)$. In other words, the length and direction of the elongation are proportional to the location of the wavefront sensing subaperture.

These elongated guidestar images complicate wavefront sensing for two reasons. First, the measurement errors associated with a given guide star signal level increases as the magnitude of the elongation grows. Secondly, unknown variations in the vertical distribution of O will introduce biases in the WFS measurement. Both of these effects are predicted to be highly significant for future, “extremely large” telescopes. The use of a noise-optimal matched filter algorithm to minimize the wavefront sensing error due to measurement noise is described in the following paragraphs. Additionally, adaptive approaches have been developed and demonstrated to track the variations

in the vertical profile of the LGS and reduce the resulting wavefront reconstruction biases to acceptable levels. See [37] for a description of this work.

3.3.1. Image Displacement Estimation via Matched Filtering Our goal is to estimate local phase gradients from WFS data in a manner that is more accurate and robust than the simple centroid scheme presented in section 2.6. According to Eq. (2.13) above, local wavefront tilts within a Shack-Hartmann WFS subaperture will have the effect of translating the nominal LGS image I_0 . Neglecting the (small) higher-order wavefront aberrations within the subaperture, we may write

$$I(\theta_{x_i}, \theta_{y_i}) = I_0(\theta_{x_i} - \delta_x, \theta_{y_i} - \delta_y) + \eta(\theta_{x_i}, \theta_{y_i}), \quad (3.9)$$

where $\boldsymbol{\delta} = (\delta_x, \delta_y)$ is the subaperture wavefront tilt to be estimated from the image I , $(\theta_{x_i}, \theta_{y_i})$ varies over the coordinates at which the image is measured by the wavefront sensor detector, and η is the (zero-mean) noise in the measurement process. For small image displacements, the dependence of \mathbf{I} upon $\boldsymbol{\delta}$ is approximately linear, yielding

$$\mathbf{I} \approx \mathbf{I}_0 + G\boldsymbol{\delta} + \boldsymbol{\eta}, \quad (3.10)$$

where

$$G = \begin{pmatrix} \frac{\partial \mathbf{I}_0}{\partial x} & \frac{\partial \mathbf{I}_0}{\partial y} \end{pmatrix} \quad (3.11)$$

and we have written the sampled images \mathbf{I} and \mathbf{I}_0 as vector quantities. The noise-optimal estimate $\hat{\boldsymbol{\delta}}$ of $\boldsymbol{\delta}$ is defined as the noise-weighted RMS best fit to the measured data according to Eq. (3.10), namely

$$\begin{aligned} \hat{\boldsymbol{\delta}} &= \arg \min_{\boldsymbol{\delta}} (\mathbf{I} - \mathbf{I}_0 - G\boldsymbol{\delta})^T C_\eta^{-1} (\mathbf{I} - \mathbf{I}_0 - G\boldsymbol{\delta}) \\ &= (G^T C_\eta^{-1} G)^{-1} G^T C_\eta^{-1} (\mathbf{I} - \mathbf{I}_0). \end{aligned} \quad (3.12)$$

Although this matched filter approach minimizes the estimation error due to measurement noise, it may suffer from limited dynamic range because the linear approximation given in Eq. (3.10) is only valid for small values of $\boldsymbol{\delta}$. This is in contrast with the standard centroid scheme (see section 2.6), which has a large linear dynamic range but is highly sensitive to measurement noise. Algorithms with intermediate properties may be defined by imposing constraints upon the optimization process. To do so, define a set \mathcal{R} of admissible operators according to

$$\mathcal{R} = \{R : RG = I, R(\mathbf{I}_i - \mathbf{I}_0) = \boldsymbol{\delta}_i\}, \quad (3.13)$$

where the shifted images \mathbf{I}_i are defined as

$$I_i(\theta_x, \theta_y) = I_0(\theta_x - \delta_{i,x}, \theta_y - \delta_{i,y}). \quad (3.14)$$

In other words, the choice of the operator is restricted to matrices which (i) are left pseudo-inverses of G , so that small image displacements will be estimated accurately in the absence of measurement noise, and (ii) are constrained to obtain the correct answer for a small number n (typically 4) of fixed image displacements $\boldsymbol{\delta}_i$. The constrained matched filter operator is then described by the formula

$$R^* = \arg \min_{R \in \mathcal{R}} \langle (R\boldsymbol{\eta})^T C_\eta^{-1} (R\boldsymbol{\eta}) \rangle, \quad (3.15)$$

where the angle brackets denote ensemble averaging over the statistics of the measurement noise $\boldsymbol{\eta}$. The matrix R^* is the minimizer of a quadratic cost function subject to linear constraints. Using Lagrange multiplier methods, it must satisfy

$$2C_\eta^{-1} R C_\eta = \Lambda M^T \quad (3.16)$$

$$RM = C, \quad (3.17)$$

where the matrices M and C have been introduced as shorthand for the following quantities:

$$M = \begin{bmatrix} G & \mathbf{I}_1 & \cdots & \mathbf{I}_n \end{bmatrix} \quad (3.18)$$

$$C = \begin{bmatrix} I & \delta_1 & \cdots & \delta_n \end{bmatrix} \quad (3.19)$$

A representation for R^* is given by the formula

$$R^* = C \left[(M^T C_\eta^{-1} M)^{-1} M^T C_\eta^{-1} \right]. \quad (3.20)$$

It is easy to confirm that $R^* M = C$, and that the formula reduces to the usual matched filter if $n = 0$ (i.e., no additional constraints are imposed upon the dynamic range of the algorithm).

References [25] and [37] contain further results on the theoretical and experimental performance of the constrained matched filter algorithm, respectively.

3.4. Advanced Concepts and Issues

A variety of advanced laser technologies and wavefront sensing concepts have been proposed to reduce or eliminate the effects of LGS elongation [13, 1] and laser pointing error [20]. These technologies are at a relatively early state of development and are outside the scope of this review. Work is also in progress to model and measure the interaction of lasers with the mesospheric sodium layer [15, 36] in order to maximize the photon return which can be achieved with a given laser power.

But the advanced concept of greatest relevance for this survey is the use of multiple laser guidestars to eliminate the “cone effect” by the application of tomographic reconstruction algorithms designed to estimate a full three-dimensional turbulence profile. We turn to this subject in detail in the following section.

4. Multi-Conjugate and Multi-Object Adaptive Optics

In section 2.2 we demonstrated that the aperture plane wavefront aberrations depend not only on position in the telescope aperture, but also on the direction of the incoming light rays; see Eq. (2.34). As a consequence, a conventional single conjugate AO system on a large telescope can provide good wavefront correction only over a very narrow range of viewing angles. The goal of multi-conjugate adaptive optics (MCAO) [5] is to provide good wavefront correction over an extended field of view.

Rather than relying on a single deformable mirror, MCAO systems make use of two or more DMs, each optically conjugate to a different height in the atmosphere. MCAO systems also require sensor input from multiple directions in order to compute DM corrections, or “figures”; see Fig. 7. At first glance, one might guess that these figures could be selected to provide extended angle wavefront correction in a manner that simply interpolates between sensed directions. However, as we pointed out in section 3, adequate wavefront sensing requires artificial beacons, which are at finite altitude. This in turn gives rise to the *cone effect*—the discrepancy between the desired wavefronts from science objects at infinity and the measured wavefronts from guidestars at finite altitudes. As a consequence, one is forced to first estimate the refractive index profile, or *atmospheric turbulence profile*, from the sensor data and then use this estimate to compute the DM figures. In section 4.1 we formally derive this 2-step process, which is very similar to the estimation-fitting decomposition of the minimum variance wavefront reconstructor which we obtained in section 2.7.

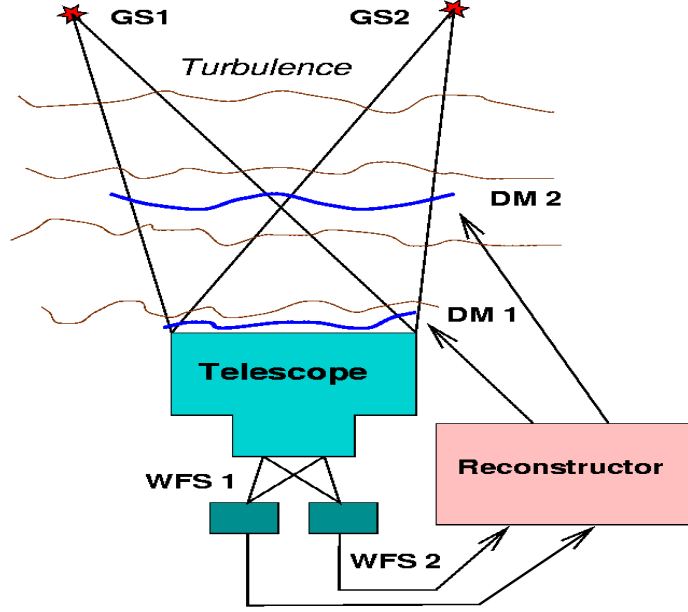


Figure 7. Schematic diagram of an MCAO system

An alternative to MCAO is multi-object adaptive optics (MOAO). In contrast to MCAO, where one desires fairly uniform wavefront correction over an extended field of view, the goal of MOAO is to obtain a high degree of wavefront correction in a few selected viewing directions, with a separate, relatively small DM dedicated to each selected direction. We will discuss MOAO in more detail in section 4.4.

4.1. MCAO wavefront reconstruction

As we pointed out in section 3.1, the tip-tilt uncertainty associated with laser guidestar sensing necessitates a mixture of laser and natural guidestar measurements. We model noise-free, open-loop LGS sensor measurements as

$$s^{\text{LGS}}(\boldsymbol{\theta}) = \begin{pmatrix} s_x^{\text{LGS}}(\boldsymbol{\theta}) \\ s_y^{\text{LGS}}(\boldsymbol{\theta}) \end{pmatrix} = \begin{pmatrix} \Gamma_x^{\text{LGS}} \\ \Gamma_y^{\text{LGS}} \end{pmatrix} P^{\text{LGS}}(\boldsymbol{\theta}) \delta n \\ \stackrel{\text{def}}{=} G^{\text{LGS}}(\boldsymbol{\theta}) \delta n. \quad (4.1)$$

Here the LGS propagation operator $P^{\text{LGS}}(\boldsymbol{\theta})$ maps the atmospheric turbulence profile δn to the aperture-plane phase via line integrals along straight-line ray paths emanating from the LGS beacon,

$$[P^{\text{LGS}}(\boldsymbol{\theta}) \delta n](x, y) = \int_0^{z_s} \delta n((1 - z/z_s)x + \theta_1 z, \\ (1 - z/z_s)y + \theta_2 z, z) dz, \quad (4.2)$$

where $(z_s \theta_1, z_s \theta_2, z_s)$ denotes beacon location. This is the analogue for finite-altitude point sources (3.1) emitting spherical waves of Eq. (2.34), which was derived from a source at infinity emitting planar waves. For convenience, we have omitted the

constant ik_0 . The x -component of the LGS sensor operator, Γ_x^{LGS} in Eq. (4.1), has a representation (2.47), and it maps the aperture-plane phase onto a vector of length equal to the number of sensor subapertures. The y -component Γ_y^{LGS} is obtained by replacing $\frac{\partial \phi}{\partial x}$ in (2.47) by $\frac{\partial \phi}{\partial y}$ and has similar mapping characteristics.

Noise-free, open-loop NGS sensor measurements have similar representations,

$$\mathbf{s}^{\text{NGS}}(\boldsymbol{\theta}) = \Gamma^{\text{NGS}} P^{\text{NGS}}(\boldsymbol{\theta}) \delta n = G^{\text{NGS}}(\boldsymbol{\theta}) \delta n. \quad (4.3)$$

The NGS propagation operator, corresponding to parallel rays resulting from a light source at infinity in direction $\boldsymbol{\theta}$, takes the form of the RHS of Eq. (2.34),

$$[P^{\text{NGS}}(\boldsymbol{\theta}) \delta n](x, y) = \int_0^H \delta n(x + \theta_1 z, y + \theta_2 z, z) dz, \quad (4.4)$$

where H is the height of the atmosphere. We represent NGS sensing operators in terms of projections onto a small number of normalized low-order modes m_k ,

$$\Gamma_k^{\text{NGS}} \phi = \int \int_{\Omega} \phi(x, y) m_k(x, y) dx dy. \quad (4.5)$$

These modes include normalized tip and tilt, which are poorly sensed by the LGS sensors.

We let the wavefront sensor operator G denote the concatenation of the $G^{\text{LGS}}(\boldsymbol{\theta})$ over a set of LGS sampling directions $\boldsymbol{\theta}$ known as the LGS asterism, and of the $G^{\text{NGS}}(\boldsymbol{\theta}')$ over directions $\boldsymbol{\theta}'$ in the NGS asterism. In place of Eq. (2.52), we employ the notation

$$\mathbf{s} = G \delta n + \boldsymbol{\eta} \quad (4.6)$$

relating the corresponding concatenated wavefront sensor data vector, sensor operator, turbulence profile, and sensor noise vector.

The wavefront fitting model from Section 2.5 also needs to be modified. Slightly generalizing Eq. (2.44), we represent the deflection of the k th DM as

$$w_k(x, y) = [A_k^{-1} F_k \mathbf{a}_k](x, y). \quad (4.7)$$

If this DM is conjugate to height z_k in the atmosphere, then the aperture-plane phase correction in direction $\boldsymbol{\theta}$ is obtained by parallel-ray propagation of w_k from z_k to the ground and is given by

$$\phi_k^{\text{DM}}(x, y; \boldsymbol{\theta}) = w_k(x + z_k \theta_1, y + z_k \theta_2) \stackrel{\text{def}}{=} [P_k(\boldsymbol{\theta}) w_k](x, y). \quad (4.8)$$

The correction from all n_{DM} mirrors is then

$$\begin{aligned} \phi^{\text{DM}}(x, y; \boldsymbol{\theta}) &= \sum_{k=1}^{n_{\text{DM}}} \phi_k^{\text{DM}}(x, y; \boldsymbol{\theta}) = \left[\sum_{k=1}^{n_{\text{DM}}} P_k(\boldsymbol{\theta}) A_k^{-1} F_k \mathbf{a}_k \right] (x, y) \\ &\stackrel{\text{def}}{=} [H(\boldsymbol{\theta}) \mathbf{a}](x, y), \end{aligned} \quad (4.9)$$

where \mathbf{a} represents the concatenation of the DM command vectors \mathbf{a}_k over all the DMs.

The wavefront reconstructor derivation from section 2.7 must also be modified. The cost functional becomes the ensemble average of the squared residual phase error, integrated over both angular field of view (FOV) and over the aperture domain Ω ,

$$\begin{aligned} J &= \left\langle \int \int_{\text{FOV}} \int \int_{\Omega} [\phi^{\text{DM}}(x, y; \boldsymbol{\theta}) - \phi^{\text{atmos}}(x, y; \boldsymbol{\theta})]^2 dx dy d\boldsymbol{\theta} \right\rangle \\ &= \left\langle \int \int_{\text{FOV}} \int \int_{\Omega} [H(\boldsymbol{\theta}) \mathbf{a} - P^{\text{NGS}}(\boldsymbol{\theta}) \delta n]^2(x, y) dx dy d\boldsymbol{\theta} \right\rangle, \end{aligned} \quad (4.10)$$

where the parallel-ray propagation operator $P^{\text{NGS}}(\boldsymbol{\theta})$ is defined in (4.4). One may also incorporate field-of-view weighting into J , e.g., if one is interested in increased resolution within a portion of the FOV.

Proceeding as in section 2.7, we assume a linear operator R which maps the concatenated sensor measurement vector \mathbf{s} from Eq. (4.6) to the concatenated actuator command vector \mathbf{a} in (4.9). The cost function J then takes the form of (2.53), but with aperture plane phase ϕ replaced by the turbulence profile δn and the identity operator I replaced by P^{NGS} . We replace Eq. (2.54) with

$$A = GC_{\delta n}G^T + C_\eta, \quad B = GC_{\delta n}(P^{\text{NGS}})^T \quad (4.11)$$

and we replace (2.55) by

$$R_{\text{MV}} = (H^T H)^{-1} H^T P^{\text{NGS}} (G^T C_\eta^{-1} G + C_{\delta n}^{-1})^{-1} G^T C_\eta^{-1}. \quad (4.12)$$

The analogue of the previously derived estimation-fitting decomposition of the reconstructor, Eq. (2.56)-(2.57), also applies. In the estimation step we solve

$$(G^T C_\eta^{-1} G + C_{\delta n}^{-1}) \delta n = G^T \mathbf{s} \quad (4.13)$$

to obtain the estimated turbulence profile δn_{MV} , and in the fitting step we solve

$$(H^T H) \mathbf{a} = H^T P^{\text{NGS}} \delta n_{\text{MV}}. \quad (4.14)$$

to obtain the desired actuator command vector.

4.1.1. Atmospheric turbulence tomography. Note that the propagation operators in Eq. (4.2) and (4.4) involve line integrals of the unknown turbulence profile along ray paths. For this reason, the estimation step (4.13) is often referred to as atmospheric turbulence tomography. The angular field of view is extremely small—on the order of a minute of arc—so the resulting tomography problem is extremely ill-posed; see [12] for analysis. The inverse covariance term $C_{\delta n}^{-1}$ has a regularizing effect which mitigates instability but filters out a significant amount of information. The estimated turbulence profile is propagated to the aperture plane before it is used in the fitting step; see the $P^{\text{NGS}} \delta n_{\text{MV}}$ term on the RHS of (4.14). The loss of (two-dimensional) aperture-plane information is much less severe than the information loss from (three-dimensional) tomography.

4.2. Other considerations

The wavefront reconstruction process for a practical MCAO system is complicated by the fact that sensor measurements are taken in “closed loop”, i.e., downstream from the DM correction. On the other hand, the previously derived minimum variance MCAO wavefront reconstruction scheme was based on the open-loop sensor model (4.6). To apply this scheme with closed-loop data, we employ a pseudo-open-loop control (POLC) approach [18, 23].

Noise-free, closed-loop NGS sensor measurements take the form

$$\mathbf{s}^{\text{NGS}}(\boldsymbol{\theta}) = \Gamma^{\text{NGS}}(P^{\text{NGS}}(\boldsymbol{\theta}) \delta n - H(\boldsymbol{\theta}) \mathbf{a}), \quad (4.15)$$

and similarly for noise-free LGS sensor measurements. Comparing the open-loop model (4.3) with the closed-loop model (4.15), we see that the two differ by the term $\Gamma^{\text{NGS}} H(\boldsymbol{\theta}) \mathbf{a}$, which represents the effects of mirror correction on sensor measurements. The key idea behind POLC is to add this term to the closed-loop NGS sensor

measurements and to add a corresponding term to the closed-loop LGS measurements before applying the MCAO wavefront reconstruction process presented in section 4.1.

Obviously the accuracy of the POLC wavefront reconstruction depends on the accuracy of the DM model. This serves as motivation for DM parameter identification in section 5.

The pseudo-open-loop actuator command vector \mathbf{a}_{POLC} must be modified before it is applied to the actuators. One first subtracts off the current DM actuator command from \mathbf{a}_{POLC} to obtain an update (this assumes linearity of the DM actuator correction operator H). One then adds to the current actuator command vector a fraction of the update, thereby implementing a concept known as proportional-integral control [7]. This can be viewed as a form of temporal filtering and it increases the robustness of the overall control scheme.

4.3. Efficient numerical implementation

We motivate this section by presenting some of the computational requirements for the Narrow-Field Infrared Adaptive Optics System (NFIRAOS) [19] for the proposed Thirty Meter Telescope. NFIRAOS will rely on 6 LGS wavefront sensors, each with a 60-by-60 subaperture array. This yields on the order of 20 thousand x-gradient measurements and 20 thousand y-gradient measurements. The number of sensor measurements associated with the NGS wavefront sensors is negligible by comparison. Hence the vector \mathbf{s} in (4.6) has approximately 40 thousand entries. NFIRAOS will have two piezo-actuated deformable mirrors—one conjugate to the ground with about 3600 actuators and the second conjugate to an altitude of 12 kilometers with about 5000 actuators. Thus the wavefront reconstruction operator R will map sensor vectors of length roughly 40 thousand to actuator vectors of length around 8600.

To accurately track the temporal evolution of the turbulence, it is necessary to perform each reconstruction in less than 500 microseconds. In addition, the reconstructor must adapt over time to changing atmospheric conditions. These considerations have led to the adoption of iterative reconstructors. We will focus on iterative techniques for system (4.13) in the MCAO estimation step. The fitting system (4.14), which is of significantly lower order, can be solved using similar methods.

Before solving (4.13) we must discretize the turbulence profile $\delta n = \delta n(x, y, z)$. Numerical simulations have shown that sufficient accuracy can be achieved with a discrete grid of size n_x -by- n_y -by- n_z with $n_z = 6$ and $n_x = n_y$ roughly equal to 160. This yields a total of about 150 thousand unknowns in the grid representation, which we denote by bold face $\delta \mathbf{n}$. We adapt the sensor model (3.4) to MCAO to obtain

$$\mathbf{s} = \begin{pmatrix} \mathbf{s}_{\text{LGS}} \\ \mathbf{s}_{\text{NGS}} \end{pmatrix} = \begin{pmatrix} G_{\text{LGS}} \\ G_{\text{NGS}} \end{pmatrix} \delta \mathbf{n} + \begin{pmatrix} \boldsymbol{\eta}_{\text{LGS}} \\ \boldsymbol{\eta}_{\text{NGS}} \end{pmatrix}. \quad (4.16)$$

The zero mean noise vectors $\boldsymbol{\eta}_{\text{LGS}}$, $\boldsymbol{\eta}_{\text{NGS}}$ have a block covariance matrix analogous to (3.5). Following [68], we take the inverse covariance in the limit as the tip-tilt uncertainty $\sigma_\theta \rightarrow \infty$, obtaining the block matrix representation

$$C_\eta^{-1} = \begin{pmatrix} C_{\text{LGS}}^{-1} - C_{\text{LGS}}^{-1/2} Q C_{\text{LGS}}^{-1/2} & 0 \\ 0 & C_{\text{NGS}}^{-1} \end{pmatrix}, \quad (4.17)$$

where Q denotes the noise-weighted orthogonal projector onto the NGS tip-tilt modes; see Eq. (3.6).

The matrix on the LHS of (4.13) can then be expressed as

$$A = A_{\text{LGS}} - A_{\text{lr}} \quad (4.18)$$

where

$$A_{\text{LGS}} = G_{\text{LGS}}^T C_{\text{LGS}}^{-1} G_{\text{LGS}} + C_{\delta n}^{-1} \quad (4.19)$$

and

$$A_{\text{lr}} = G_{\text{LGS}}^T C_{\text{LGS}}^{-1/2} Q C_{\text{LGS}}^{-1/2} G_{\text{LGS}} - G_{\text{NGS}}^T C_{\text{NGS}}^{-1} G_{\text{NGS}}. \quad (4.20)$$

Matrix A_{lr} has relatively small rank equal to the rank of Q plus the rank of G_{NGS} , which equals the number of NGS modes m_k in (4.5). Hence the subscript “lr” for “low rank”. On the other hand, A_{LGS} has rank equal to the number grid points in the turbulence profile representation.

Given a means of inverting A_{LGS} , several approaches may be taken to invert the A in (4.18). By applying the Sherman-Morrison formula [27], also known as the matrix inversion lemma, one can express the inverse of A as the inverse of A_{LGS} plus a low rank perturbation derived from A_{lr} and A_{LGS}^{-1} . A second approach is to base a preconditioner for A on a preconditioner derived for A_{LGS} alone. This is appealing for theoretical reasons, as the asymptotic convergence rate of conjugate gradient iteration is not affected by low-rank perturbations. A third alternative, presented in section 4.3.1, avoids the low rank perturbation. In any event, one needs an efficient scheme to invert A_{LGS} .

We now examine the structure of A_{LGS} in more detail, again relying on NFIRAOS guidelines. Corresponding to the $n_z = 6$ vertical partitions, or “layers”, in the discretization of δn , A_{LGS} has an n_z -by- n_z block representation with blocks

$$A_{k\ell} = \sum_j P_k^T(\theta_j) \Gamma^T C_{\text{LGS},j}^{-1} \Gamma P_\ell(\theta_j) + \delta_{k\ell} C_{\delta n,k}^{-1}. \quad (4.21)$$

For convenience we have dropped the subscript LGS from the A . The indices j in the sum range over the laser guide star directions (6 total for NFIRAOS). $C_{\text{LGS},j}$ denotes the j th diagonal block of the LGS noise covariance matrix, which has a block diagonal representation due to noise independence over the different LGS directions. Similarly, the atmospheric turbulence covariance matrix $C_{\delta n}$ is block diagonal, since the turbulence layers are assumed to be independent; hence the term $\delta_{k\ell} C_{\delta n,k}^{-1}$, where $\delta_{k\ell}$ is the Kronecker delta. The matrices $P_\ell(\theta_j)$ represent LGS propagation from atmospheric turbulence layers ℓ to the aperture plane in directions θ_j . These can be obtained from discretization of (4.2). The matrix Γ is a discrete concatenation of sensor operators Γ_x^{LGS} and Γ_y^{LGS} ; see (4.1) and (2.47).

By employing straightforward discretization schemes, each of the matrices $P_\ell(\theta_j)$, Γ , and $C_{\text{LGS},j}^{-1}$ in (4.21) has a very sparse representation, but the matrices $C_{\delta n,k}^{-1}$ do not. In addition, all the matrices in (4.21) except $C_{\text{LGS},j}^{-1}$ have diagonal Fourier-domain representations. Recall from section 2.3 that the atmospheric turbulence covariance has a power spectrum which decays asymptotically as $\kappa^{-11/3}$, where κ denotes wave number. Hence the inverse covariance power spectrum grows as $\kappa^{11/3}$. Motivated by the fact that $\kappa^{11/3} \approx \kappa^4$, which is the spectral growth rate for the biharmonic (squared Laplacian) operator, Ellerbroek [17] proposed a (sparse) scaled discrete biharmonic approximation to the inverse turbulence covariance matrix. If we replace the $C_{\delta n,k}^{-1}$ by scaled discrete biharmonics, each of the component matrices in (4.21) are sparse and sparse iterative methods [57] can be applied.

Note that system (4.13) is symmetric positive definite, so conjugate gradient (CG) iteration may be applied to solve it. This system is quite ill-conditioned and CG convergence tends to be quite slow. The same holds for systems involving the “LGS-reduced matrix” A_{LGS} in Eq. (4.19). For this reason, considerable effort has been

put into the search for effective preconditioners. Gilles et al [24] proposed a multigrid [62] preconditioned CG scheme. Yang et al proposed a Fourier domain preconditioner [68]. Very rapid convergence has been demonstrated for both of these preconditioned CG schemes [26]. However, both approaches have significant overhead costs. The traditional cost metric in computational mathematics has been the number of floating point operations required to solve a system. This metric suggests that significant gain can be achieved from preconditioning. However, the only way to achieve NFIRAOS goals with current computer hardware is to distribute the computations across multiple processors. Unfortunately, both multigrid and Fourier domain preconditioners have prohibitively high overhead costs in terms of the time required for inter-processor communications. It should be noted that these considerations may change with advances in computer hardware.

An attractive alternative is to use CG iterations without any preconditioning. For this particular problem, the high spatial frequency components of the residual solution error decrease quite rapidly with CG iteration, while the low spatial frequency components persist. CG iterations are performed within a control scheme that can be viewed as a time discretization; see section 4.2. High spatial frequency components of the turbulence evolve much more rapidly than do components of low frequency. By employing “warm restart” (i.e., by taking the last CG iterate from the previous time step as the initial guess for the current time step), we can take advantage of the match between CG convergence behavior and the temporal evolution of the turbulence. Interprocessor communication cost for CG is also relatively low, as is its algorithmic complexity.

4.3.1. Split tomography In practice, the estimation of the atmospheric turbulence profile δn from a joint vector \mathbf{s} of both laser- and natural-guide star WFS measurements as prescribed in Eq. (4.13) creates a variety of complications for implementation. The dimensionality of the LGS WFS measurement vector is very large, the signal-to-noise ratio on these measurements is (relatively) high, the geometry of the LGS asterism is fixed, and these measurements are used to control all but a few of the deformable mirror degrees of freedom. In comparison, the dimensionality of the NGS WFS measurements is very small, their signal to noise ratio may be much lower, the geometry and brightness of the NGS asterism varies from observation to observation, and these measurements are used to control only a few deformable mirror degrees of freedom which are unobservable using the LGS WFS. Decoupling the DM control problem into separate LGS- and NGS-controlled subspaces simplifies the formulation of computationally efficient approaches for the LGS-controlled modes, and also allows for rapid updating of the low-dimensional NGS control algorithm as the NGS asterism varies or observing conditions change. In (simulated) practice, there is little or no reduction in performance associated with this partitioning.

To briefly outline the implementation of this “split tomography” concept, we decompose the space \mathcal{A} of DM actuator commands as the orthogonal sum $\mathcal{A} = \mathcal{A}_{\text{LGS}} \oplus \mathcal{A}_{\text{NGS}}$. Here \mathcal{A}_{NGS} is a low-dimensional subspace of DM actuator commands which are unobservable to the LGS wavefront sensors, and \mathcal{A}_{LGS} is its orthogonal complement. Note that the existence of a non-trivial subspace of DM actuator commands in the null space of the LGS wavefront sensors occurs because the tip/tilt (or image motion) component of each LGS WFS measurement is uncertain. Each vector $\mathbf{a}_{\text{NGS}} \in \mathcal{A}_{\text{NGS}}$ introduces a tip/tilt error in the wavefront propagated from each

laser guidestar, but no higher-order wavefront aberration.[‡]

With this decomposition of the space of DM actuator commands, the formulas for the WFS measurement vectors \mathbf{s}_{LGS} and \mathbf{s}_{NGS} become

$$\begin{aligned}\mathbf{s}_{\text{LGS}} &= G_{\text{LGS}}\delta n + G'_{\text{LGS,LGS}}\mathbf{a}_{\text{LGS}} + \boldsymbol{\eta}_{\text{LGS}} \\ \mathbf{s}_{\text{NGS}} &= G_{\text{NGS}}\delta n + \begin{pmatrix} G'_{\text{NGS,LGS}} & G'_{\text{NGS,NGS}} \end{pmatrix} \begin{pmatrix} \mathbf{a}_{\text{LGS}} \\ \mathbf{a}_{\text{NGS}} \end{pmatrix} + \boldsymbol{\eta}_{\text{NGS}}.\end{aligned}\quad (4.22)$$

Here $G'_{\text{xGS,yGS}}$ represent the influence function from either the NGS or LGS space of DM actuator commands into the NGS or LGS WFS measurement; note that $G'_{\text{LGS,NGS}} \equiv 0$ due to the assumption that the NGS-controlled subspace \mathcal{A}_{NGS} of \mathcal{A} lies within the null space of the LGS WFS. This decomposition suggests that it might be acceptable to determine \mathbf{a}_{LGS} from \mathbf{s}_{LGS} using Eqs. (4.13) and (4.14), where (i) the quantities G , $\boldsymbol{\eta}$, and \mathbf{s} are subscripted by “LGS” in equation (4.13), and (ii) the influence matrix H is restricted to the subspace \mathcal{A}_{LGS} in Eq. (4.14).

The approach to determining \mathbf{a}_{NGS} is more difficult to rigorously justify. Numerical simulations indicate that a straightforward, noise-weighted least squares algorithm of the form

$$\Delta\mathbf{a}_{\text{NGS}} = [(G'_{\text{NGS,NGS}})^T C_{\eta_{\text{NGS}}}^{-1} (G'_{\text{NGS,NGS}})]^{-1} (G'_{\text{NGS,NGS}})^T C_{\eta_{\text{NGS}}}^{-1} \mathbf{s}_{\text{NGS}} \quad (4.23)$$

obtains good results in practice. The notation $\Delta\mathbf{a}_{\text{NGS}}$ denotes that this is an incremental estimate of the error in the current value of the command \mathbf{a}_{NGS} based upon the closed-loop (i.e., corrected by the current value of the DM command) value of the NGS WFS measurement vector.

Heuristically, split tomography represents a generalization to MCAO of the standard control approach currently utilized in LGS AO system, where the tip/tilt component of the wavefront is controlled using the single NGS WFS measurement, and the higher-order DM command is computed based upon the LGS WFS. For MCAO, the dimension of the NGS-control actuator command vector \mathbf{a}_{NGS} is enlarged to include a number of deformable mirror modes which shift the apparent position of each LGS, but introduce no higher-order wavefront aberration. See [26] for further description and sample simulation results for split atmospheric tomography.

4.4. Multi-object adaptive optics (MOAO)

In principle, the field-of-view over which atmospheric turbulence may be compensated via MCAO can be made arbitrarily large via the use of an arbitrary number of deformable mirrors placed in series. In practice, the effective limit on the number of DMs is typically 2 or 3 before the penalties of increased cost, reduced optical throughput, and complex opto-mechanical packaging begin to outweigh the benefits obtained. *Multi-Object Adaptive Optics*, or MOAO, is a more recent and innovative approach to broadening the corrected field-of-view which has been proposed to overcome this limitation for applications where a large number of small, widely separated objects (such as distance galaxies) are to be observed using adaptive optics. MOAO provides entirely separate wavefront corrections for each of these objects by using multiple deformable mirrors in parallel, so that the number of optical surfaces

[‡] Also, the Hilbert Space inner product which is implicit in this decomposition of the actuator command space \mathcal{A} is defined in terms of the wavefront corrections applied by the DM actuator command vectors at one or several points in the field-of-view.

in each path need no longer increase with the size of the compensated field-of-view [2].

A variety of practical implementation issues must be resolved to implement an MOAO system. In particular, the wavefront sensing and correcting channels are separated in MOAO, so that the wavefront sensors are required to sense the full amplitude of the turbulence-induced wavefront distortion with high accuracy. Similarly, the deformable mirrors are required to implement large wavefront corrections without real-time optical feedback on the actuator commands which have actually been applied. Highly accurate calibration of wavefront sensors and deformable mirrors is consequently essential for MOAO. Additionally, the deformable mirrors used for MOAO must be relatively inexpensive (because of their multiplicity) and sufficiently small to be flexibly deployed to match the locations of the science targets in each field-of-view selected by the astronomer. It is anticipated that all of these wavefront corrector challenges can be overcome through the use of MEMS deformable mirrors.

On the other hand, the algorithmic requirements associated with MOAO are no more difficult than for MCAO, and in some aspects are even simpler. Both approaches utilize tomographic wavefront reconstruction to estimate a 3-dimensional atmospheric turbulence profile using wavefront sensor measurements from multiple laser- and natural guidestars. However, Pseudo-open loop control (POLC) need not be implemented for MOAO because the WFS measurements are actually obtained in open loop. Secondly, both approaches apply a fitting step to estimate the DM actuator commands which optimally compensate the turbulence-induced wavefront distortion according to Eq. (4.14) above. Because the DMs in an MOAO system operate in parallel, the DM influence matrix H is given by $H = \text{diag}(H_1, \dots, H_n)$, where n is the number of science objects and each H_i takes a common value H_0 according to the parameters of the DM duplicated in each science channel.

5. Parameter Identification for Deformable Mirrors

In section 2.4 we derived the simple 2-parameter DM model equation (2.42). In this section we discuss extensions to this model and address the identification of model parameters. This discussion is motivated primarily by the need for very precise open-loop DM control that arises in Multi-Object Adaptive Optics (MOAO), which we discussed in section 4.4.

Most current astronomical AO systems use DMs with piezo-stack actuators. The facesheets for these DMs are relatively thick and quite uniform, so the facesheet model (2.37) is very accurate. In addition, actuators which are not malfunctioning tend to be very uniform, and piezo-ceramic materials have been well characterized [33]. Fig. 3 shows an influence function for a particular DM which was manufactured by CILAS [58] and utilizes piezo-stack actuators that are composed of lead zirconate titanate, or PZT. If they have not been previously activated, PZT actuators display a nearly linear voltage response. In this case the linearized actuator model (2.41) is very accurate, as is the 2-parameter DM model (2.42). We were able to obtain a very good fit to measured data obtained from the CILAS DM by simple “hand calibration” of the two parameters; see solid and dashed curves in the bottom plot in Fig. 3.

Unfortunately, piezo actuators are subject to hysteresis—the dependence of the current voltage response on the past voltage history. For this reason, piezo-activated DMs are not suitable for high-precision open-loop operation. Extremely

precise, stable, repeatable wavefront correction has recently been demonstrated using electrostatically actuated MEMS DMs [46]. These devices are relatively inexpensive; they can achieve very high actuator density; they are not subject to viscoelastic creep—hence the stability; and they are not subject to hysteresis—hence the repeatability. However, other characteristics of these DMs make modeling and control quite difficult. There may be a relatively high degree of inter-actuator variability, and at large displacements, nonlinearity of the actuator response function becomes significant.

5.1. Inter-actuator variability

To account for inter-actuator variability, we can replace (2.38) by

$$z_i = r_i(p_i, V_i), \quad i = 1, \dots, n_a, \quad (5.1)$$

to obtain

$$\nabla^4 w + \sum_{i=1}^{n_a} \beta_{1,i} w(\mathbf{x}_i) \delta(\mathbf{x} - \mathbf{x}_i) = \sum_{i=1}^{n_a} \beta_{2,i} a_i \delta(\mathbf{x} - \mathbf{x}_i), \quad (5.2)$$

where now

$$\beta_{1,i} = 1/D_{\text{fs}} \frac{\partial r_i}{\partial p}(0, \bar{V}), \quad \beta_{2,i} = \frac{\partial r_i}{\partial V}(0, \bar{V}) \beta_{1,i}. \quad (5.3)$$

We have also relabeled the ΔV_i as a_i . We can express this in operator form as

$$A(\beta_1)w = F(\beta_2)\mathbf{a}. \quad (5.4)$$

Note that the parameter-dependent linear operator $A(\beta_1)$, defined by the LHS of (5.2), is self-adjoint.

A standard approach to the identification of parameters in differential equations is the method of output least squares (OLS); see [63]. In this context, one selects parameter vectors $\beta_1 = (\beta_{1,i}), i = 1, \dots, n_a$ and $\beta_2 = (\beta_{2,i}), i = 1, \dots, n_a$ to minimize

$$J_{\text{OLS}}(\beta_1, \beta_2) = \frac{1}{2} \int \int [w(x, y; \beta_1, \beta_2, \mathbf{a}) - w_{\text{obs}}(x, y; \mathbf{a})]^2 dx dy. \quad (5.5)$$

Here the integration is performed over the horizontal extent of the facesheet; $w(x, y; \beta_1, \beta_2, \mathbf{a})$ denotes the solution of (5.2) for a fixed actuator command vector \mathbf{a} and fixed parameter vectors β_1 and β_2 ; and $w_{\text{obs}}(x, y; \mathbf{a})$ represents observed DM facesheet displacement obtained from an experiment in which the same actuator command vector \mathbf{a} is applied. If measurements are taken at discrete points, the integral in (5.5) is replaced by a discrete sum. If m experiments are performed, we may replace the RHS of (5.5) with a sum of m terms, each form of the RHS, but with \mathbf{a} replaced by corresponding actuator command vectors $\mathbf{a}_k, k = 1, \dots, m$.

Typical numerical minimization schemes require the gradient of J_{OLS} . Using adjoint, or costate, methods [63], an entire output least squares gradient computation can be performed with only 2 PDE solves—one to obtain the “state variable” w from Eq. (5.2), and a second to obtain the “costate variable” u from a related equation. This is particularly important in mirror characterization for DMs that may have hundreds or thousands of actuators.

The OLS gradient $\mathbf{g} = \nabla J_{\text{OLS}}$ is a $2n_a$ -component vector which we can decompose as $\mathbf{g} = (\mathbf{g}_1, \mathbf{g}_2)$, where for $k = 1, 2$,

$$[\mathbf{g}_k]_i = \frac{\partial J_{\text{OLS}}}{\partial \beta_{k,i}}, \quad i = 1, \dots, n_a.$$

The costate approach yields components of the gradient with respect to β_1 in terms of an L^2 inner product,

$$[\mathbf{g}_1]_i = (DA(\beta_1; \mathbf{e}_i)w, u)_{L^2}. \quad (5.6)$$

Here the state variable w solves (5.2); the costate variable u is the solution to the adjoint equation

$$A(\beta_1)u \stackrel{\text{def}}{=} \nabla^4 u + \sum_{i=1}^{n_a} \beta_{1,i} u(\mathbf{x}_i) \delta(\mathbf{x} - \mathbf{x}_i) = -r(\mathbf{x}), \quad (5.7)$$

where the residual $r = w - w_{\text{obs}}$; and $DA(\beta_1; \mathbf{e}_i)$ denotes the Gateaux derivative of A at β_1 in the direction of the i th standard n_a -component unit vector; see (1.7). From (5.2) we see that

$$DA(\beta_1; \mathbf{e}_i)w = w(\mathbf{x}_i)\delta(\mathbf{x} - \mathbf{x}_i),$$

so that (5.6) simplifies to

$$[\mathbf{g}_1]_i = w(\mathbf{x}_i)u(\mathbf{x}_i), \quad i = 1, \dots, n_a. \quad (5.8)$$

Gradient components with respect to β_2 can be obtained in an analogous manner.

$$\begin{aligned} [\mathbf{g}_2]_i &= (A(\beta_1)^{-1} DF(\beta_2; \mathbf{e}_i)\mathbf{a}, r)_{L^2} \\ &= (a_i \delta(\mathbf{x} - \mathbf{x}_i), A(\beta_1)^{-1} r)_{L^2} \\ &= -a_i u(\mathbf{x}_i), \end{aligned} \quad (5.9)$$

where again the costate variable u solves the adjoint equation (5.7).

5.2. Nonlinear actuator response

To gain insight into actuator nonlinearities, we review the MEMS DM model introduced in [65]. The device considered in that paper has electrostatic actuators consisting of small plates suspended above a polysilicate base. These plates are connected to the facesheet by rigid posts. Ignoring material and structural variations among the actuators, we take the actuator plate displacement $z(\mathbf{x}')$ to be the solution to the PDE

$$D_{\text{act}} \nabla^4 z - p_i \delta(\mathbf{x}' - \mathbf{0}) = \frac{\epsilon_0 \epsilon_r V_i^2}{(g - z(\mathbf{x}'))^2}. \quad (5.10)$$

Here \mathbf{x}' denotes horizontal position in a local actuator coordinate system whose origin $\mathbf{0}$ is the location of the connecting post; the gap size parameter g represents the distance between the unforced actuator plate and the base substrate; ϵ_0 denotes free-space permittivity; ϵ_r is the dielectric constant of the gap media; and D_{act} denotes the flexural rigidity of the actuator plate.

As in Section 2.4, p_i denotes the point load on the DM facesheet at post location \mathbf{x}_i , which due to the rigid post, matches the point load at the origin of the actuator plate coordinate system, and V_i denotes the actuator control voltage. The actuator response function $r(p, V)$ is defined to be $z(\mathbf{0}; p, V)$, the solution to (5.10) with $p = p_i$ and $V = V_i$ evaluated at the origin.

The squared voltage term V_i^2 on the RHS of (5.10) constitutes a nonlinearity which can be removed simply by defining a_i to be proportional to V_i^2 . A non-removable nonlinearity comes from the denominator on the RHS, which arises from the inverse square law relating the force between parallel charged plates. When the actuator plate displacement approaches the gap parameter g , this nonlinearity becomes more

pronounced. The parallel plate condition also becomes less reasonable in this case. In addition, large displacements may induce stretching in the actuator plate, which introduces an additional nonlinearity which is not accounted for in (5.10).

Given the model (5.10), one might consider applying output least squares to estimate the parameters D_{act} , g , and $\epsilon_0\epsilon_r$. In light of modeling uncertainties, a more prudent approach would be to represent $r(p, a)$, with $a = V^2$, in terms a bivariate spline (piecewise polynomial in p and a) and then to apply OLS to estimate the coefficients of the spline. An analysis of (5.10) suggests that the spline representation could be relatively simple. For instance, when $a = V^2 = 0$, this PDE is linear in p_i . In addition, for displacements z which are small relative to the gap g ,

$$a(g - z)^{-2} \approx g^{-2}a + 2g^{-3}az. \quad (5.11)$$

Hence one might expect the solution to (5.10), and hence $r(p, a)$, to be approximately linear in a as well as approximately linear in p , but not approximately jointly linear in p and a .

An alternative approach to MEMS actuator parameter identification is presented by Stewart et al [59]). These authors used the equation error method [3] to obtain a point load $p = p_i$ from measured DM displacement data through a variant of the facesheet model (2.37). By varying (squared) voltage across a specified collection of actuators, they obtained a collection of data triples (p_i, z_i, a_i) . They then assumed a parametric form $p = f(z, a)$, which was based on a simplified version of the actuator equation (5.10) in which they replaced the biharmonic term by $k_A z$, where the parameter k_A plays the role of a spring constant. Finally, they employed a nonlinear least squares scheme to fit the model parameters g , k_A , and $\epsilon_0\epsilon_r$ to the data triples. The authors attributed control errors from their scheme to inter-actuator variability. It is possible that the extensive filtering required to mitigate the effects of taking 4 derivatives of measured data may also have contributed to the reported control error.

5.3. Deformable secondary mirrors

The secondary mirror is a second light gathering and focusing surface in a reflecting telescope. Light gathered by the primary mirror is directed towards a focal point typically past the location of the secondary. The secondary mirror directs the light either to the side (Newtonian reflector) or back towards a focal point behind and through the primary (Cassegrain reflector). AO can then be applied to the reflected light. It is desirable to minimize the number of reflections, since at each reflection some of the light is lost. Moreover, when imaging in the near infrared, reflective surfaces radiate heat, thereby introducing additional noise. This has motivated the incorporation of adaptive optics correction in the secondary mirror [8, 52].

Deformable secondary mirrors (DSMs) are, at least in principle, very similar to the DMs discussed previously. However, there are some important practical differences. The unactuated facesheet of a DSM has a hyperboloidal or ellipsoidal surface, rather than the flat surface of a conventional DM. For this reason, facesheet models rely on thin shell theory rather than thin plate theory. In addition, existing DSMs are separated from a rigid support by a cushion of air, and magnetic voice-coil actuators attached to the back of these DSMs are used to induce surface deformations. This approach provides for structural stability and stiffness at all frequencies of vibration. Capacitive sensors attached to the actuators allow one to precisely measure the facesheet deformations with respect to the support at the actuator locations. This

provides feed-back for a local closed-loop control scheme which can be used to precisely position the DSM at the actuators.

Given precise feed-back control, there is still a need for additional modeling and parameter identification. For example, unknown variations in the position of the rigid support structure will give rise to non-random, but unknown “systematic” wavefront errors. Hence there is interest in modeling and estimating the effect of gravity and temperature variations on the secondary mirror’s support structure. In addition, there is a need to understand, model, and estimate the (temporal) dynamics of the DSM. This is required to reduce the time needed for the controller to respond to a given input, because atmospheric turbulence evolves on time scales that may be comparable to the time scales of the mirror dynamics.

We now move to a new topic, separate but mathematically interesting and of great current interest in astronomy.

6. High-Contrast Imaging and Adaptive Optics

With the advent of adaptive optics, the angular resolution of large, ground-based telescopes is now theoretically sufficient to enable the direct detection of extra-solar planets orbiting nearby stars. The development of such *high-contrast imaging* systems has become one of the most active subjects in astronomical AO, but their successful design and implementation remains very challenging. The contrast ratio between a star and its planet(s) is estimated to be on the order of 10^{-7} to 10^{-9} , with an angular separation between the two objects of only a few λ/D , where λ is the wavelength of the light and D is the diameter of the telescope’s primary mirror. Under these conditions, the scattered and diffracted light from the star must be minimized to obtain a non-negligible signal-to-noise ratio, even assuming that atmospheric turbulence and other sources of wavefront distortion can be fully corrected by an effectively perfect AO system.

Coronagraphy is one standard approach proposed for this purpose. A coronagraph consists of a series of masks and apodizers (i.e., non-uniform optical transmittance functions), which are placed in image and pupil planes to both block the central core of the star image and simultaneously attenuate the amount of the diffracted light. Subsections 6.1 and 6.2 below provide an introduction to the basic theory of an apodized pupil Lyot coronagraph, which is one specific instance of this general approach. In particular, we outline a derivation for determining the functional form of the optimal pupil plane apodizer, namely the so-called circular prolate function.

Next, subsection 6.3 briefly discusses the impact of residual wavefront aberrations upon the performance of a high contrast imaging system. To first order, there is a direct 1-1 correspondence between the spatial frequency of a wavefront error and the location of the “speckle” it produces in the image plane. The proper AO performance metric for high contrast imaging is therefore not simply the Strehl ratio which is obtained, but instead the magnitude of the residual wavefront errors in a specified spatial frequency passband. This is a very important result for specifying the performance requirements for wavefront sensors and deformable mirrors.

Finally, subsection 6.4 gives brief outline of Fourier transform wavefront reconstruction methods for high contrast imaging AO. Explicitly estimating the individual Fourier modes of the wavefront distortion profile is one approach to reducing the computation requirements for high-order wavefront reconstruction, and may also

prove useful for implementing predictive control.

6.1. Apodized Pupil Lyot Coronagraphy

Fig. 8 defines the notation and basic elements of the Apodized Pupil Lyot Coronagraph (APLC) to be studied in this section. The figure consists of four planes, and the scalar wave electric fields of the starlight in these planes will be written as U_1 , u_2 , U_3 , and u_4 . Planes number 1 and 3 are pupil planes of the optical system, while 2 and 4 are the image planes (the relay optics between the four planes are not shown). It is customary in coronagraphy to represent pupil plane coordinates by \mathbf{r} and image plane coordinates by $\boldsymbol{\theta}$. We will assume that these coordinates have been scaled such that the far-field wavefront propagator from pupil to image plane is simply the two-dimensional Fourier transform \mathcal{F} . To simplify the notation, the Fourier transform of a function $M(\mathbf{r})$ defined on a pupil plane will be represented as the lower case function $m(\boldsymbol{\theta})$, and conversely for the inverse Fourier transform.

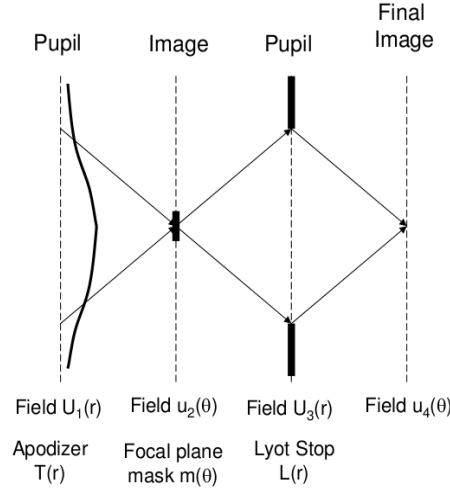


Figure 8. Schematic layout for an apodized pupil Lyot Coronagraph, and associated notation for the scalar electric fields at each pupil and image plane.

The starlight entering the system in plane number 1 at the left of the figure has an electric field given by $P(\mathbf{r}) \exp[i\phi(\mathbf{r})]$, where $P(\mathbf{r})$ is a fixed $\{0, 1\}$ -valued amplitude function and $\phi(\mathbf{r})$ is the (small) residual wavefront error left uncorrected by the AO system. Planes number 1 through 3 then contain a series of aperture stops or apodizers designed to prevent starlight from reaching the final focal plane and improve the odds of detecting a faint stellar companion. These stops are:

- A focal plane mask $m(\boldsymbol{\theta})$ in plane number 2, which simply blocks the central core of the star image;

- A Lyot stop $L(\mathbf{r})$ in plane number 3, which was introduced by Lyot [41] to block the diffraction pattern produced by $m(\boldsymbol{\theta})$ near the edge of the pupil; and
- A pupil plane apodizer $T(\mathbf{r})$ in plane number 1, which can be chosen to maximize the fraction of the star's energy blocked by the focal plane mask $m(\boldsymbol{\theta})$ in plane number 2. We can assume that $0 \leq T(\mathbf{r}) \leq P(\mathbf{r})$.

We will show below that the proper choice for L is given by $L = P$ if the pupil plane apodizer $T(\mathbf{r})$ has been chosen optimally. In this case, the propagation of starlight from plane to plane through the Lyot Coronagraph is described by the following equations:

$$U_1(\mathbf{r}) = T(\mathbf{r})P(\mathbf{r}) \exp[i\phi(\mathbf{r})] = T(\mathbf{r}) \exp[i\phi(\mathbf{r})], \quad (6.1)$$

$$u_2(\boldsymbol{\theta}) = [1 - m(\boldsymbol{\theta})]u_1(\boldsymbol{\theta}), \quad (6.2)$$

$$U_3(\mathbf{r}) = P(\mathbf{r})U_2(\mathbf{r}), \quad (6.3)$$

$$u_4(\boldsymbol{\theta}) = u_3(\boldsymbol{\theta}). \quad (6.4)$$

We wish to determine an optimal pupil plane apodizing function, $T_*(\mathbf{r})$, which will maximize the fraction of the starlight blocked by the focal plane mask $m(\boldsymbol{\theta})$, subject to the constraint that the total energy passed through the apodizer is equal to some constant C . We consider the ideal case of a perfect AO system which has nulled the residual wavefront aberration $\phi(\mathbf{r})$, so that $U_1(\mathbf{r}) = T(\mathbf{r})$. The formal solution to the maximization problem is then given by

$$T_* = \arg \max_{T \in \mathcal{T}} \int \int |t(\boldsymbol{\theta})|^2 m(\boldsymbol{\theta}) d\boldsymbol{\theta}, \quad (6.5)$$

$$\mathcal{T} = \{T : 0 \leq T(\mathbf{r}) \leq P(\mathbf{r}), \|T\|_2^2 = C\}. \quad (6.6)$$

A variational argument can be used to demonstrate that the convolution product $T_* * M$ must be equal to a constant multiple of T_* almost everywhere on $\text{supp } P$, the support of the pupil function P . In particular, Eq. (6.1) implies

$$\int \int |t_*(\boldsymbol{\theta}) + \delta(\boldsymbol{\theta})|^2 m(\boldsymbol{\theta}) d\boldsymbol{\theta} \leq \int \int |t_*(\boldsymbol{\theta})|^2 m(\boldsymbol{\theta}) d\boldsymbol{\theta} \quad (6.7)$$

for any perturbation Δ to the apodizer function on $\text{supp } P$ which satisfies $\|T_* + \Delta\|_2^2 = \|T_*\|_2^2$. Replacing Δ by $\epsilon\Delta$ and letting $\epsilon \rightarrow 0$, we obtain

$$(T_* * M, \Delta) = \int \int [t_*(\boldsymbol{\theta})m(\boldsymbol{\theta})] \delta^*(\boldsymbol{\theta}) d\boldsymbol{\theta} = 0 \quad (6.8)$$

whenever $(T_*, \Delta) = 0$. In other words, $T_* * M$ is orthogonal to all functions in $L^2(\text{supp } P)$ which are orthogonal to T_* , so $T_* * M$ must lie in the 1-dimensional span of this vector. We write

$$T_* * M = \Lambda T_* \quad (6.9)$$

in the sense of functions in $L^2(\text{supp } P)$.

We now continue propagating the starlight to the final focal plane in the case of the optimal apodizer T_* . From Eqs. (6.2) through (6.4), it follows that

$$U_3(\mathbf{r}) = (1 - \Lambda)T_*(\mathbf{r}), \quad (6.10)$$

$$u_4(\boldsymbol{\theta}) = (1 - \Lambda)t_*(\boldsymbol{\theta}). \quad (6.11)$$

Finally, the fraction of the starlight which “leaks” outside of the masked region $m(\boldsymbol{\theta})$ in the final focal plane image is given by

$$\begin{aligned} \int \int |u_4(\boldsymbol{\theta})|^2 [1 - m(\boldsymbol{\theta})] d\boldsymbol{\theta} &= (1 - \Lambda)^2 (T_* - M * T_*, T_*) \\ &= (1 - \Lambda)^3 \|T_*\|_2^2. \end{aligned} \quad (6.12)$$

Clearly, rejecting a large fraction of the starlight depends upon obtaining a solution T_* with a value of Λ which is close to unity.

6.2. Results for a Circular Pupil and Focal Plane Mask

To proceed further, we consider the special case of a pupil function P and focal plane mask m defined by

$$P(\mathbf{r}) = \Pi(\mathbf{r}/D), \quad (6.13)$$

$$m(\boldsymbol{\theta}) = \Pi(\boldsymbol{\theta}/a), \quad (6.14)$$

where $\Pi(\mathbf{x})$ is the characteristic function of a disk with unit diameter. Eq. (6.9) now becomes

$$\Pi(\mathbf{r}/D)\mathcal{F}^{-1}[\mathcal{F}(T_*)\Pi(\boldsymbol{\theta}/a)] = \Lambda T_*(\mathbf{r}). \quad (6.15)$$

If we restrict attention to radially symmetric solutions given by $T_*(\mathbf{r}) = \Psi(|\mathbf{r}|)$, the two-dimensional Fourier transforms may be reduced to Hankel transforms, yielding the result

$$\Pi(\mathbf{r}/D)(2\pi)^2 \int_0^{a/2} \theta \left[\int_0^{D/2} s \Psi(s) J_0(2\pi s \theta) ds \right] J_0(2\pi \theta |\mathbf{r}|) d\theta = \Lambda \Psi(|\mathbf{r}|). \quad (6.16)$$

We wish to reduce this double integral to an iterated integral operator in order to solve for Ψ . From the changes of variable $\theta' = \sqrt{D/a}\theta$, $s' = \sqrt{a/D}s$, and $\mathbf{r}' = \sqrt{a/D}\mathbf{r}$, it follows that the function $f(\mathbf{x}) = \Psi(\sqrt{D/a}|\mathbf{x}|)$ satisfies the relationship

$$H^2 f = \Lambda f, \quad (6.17)$$

where the operator H is given by

$$(Hg)(\mathbf{x}) = \Pi(\mathbf{x}/\sqrt{aD}) \int_0^{\sqrt{aD}/2} 2\pi x' g(x') J_0(2\pi |\mathbf{x}| x') dx'. \quad (6.18)$$

The operator H is Hermitian on $L^2([0, \sqrt{aD}/2], \mu)$ with respect to the measure $\mu(y) = 2\pi y dy$, so Eq. (6.17) implies $Hf = \Lambda^{1/2}f$. Equivalently,

$$\Pi(\mathbf{r}/a) \int_0^{D/2} 2\pi s \Psi(s) J_0(2\pi s |\mathbf{r}|) ds = \left(\frac{D}{a}\right) \Lambda^{1/2} \Psi(D|\mathbf{r}|/a). \quad (6.19)$$

The solutions Ψ to this integral equation are the so-called *circular prolate* functions. Further details on their computation are outside the scope of this survey. See [38] for additional information.

Finally, reference [39] describes extensions of these results to cases of more general pupil functions P , focal plane masks m , and broadband imaging over a nonzero spectral passband.

6.3. Effect of Residual Wavefront Aberrations

The results presented in sections 6.1 and 6.2 above are for the ideal case of perfect AO wavefront compensation. In practice, the residual wavefront error $\phi(\mathbf{r})$ will be small but nonzero. In this case, the formula for the complex amplitude function $U_1(\mathbf{r})$ in the first pupil plane becomes

$$\begin{aligned} U_1(\mathbf{r}) &= T_*(\mathbf{r}) \exp[i\phi(\mathbf{r})] \\ &= T_*(\mathbf{r}) [1 + i\phi(\mathbf{r}) + O(\phi^2)]. \end{aligned} \quad (6.20)$$

The first-order effect upon the field $u_2(\boldsymbol{\theta})$ in the plane of the following focal mask is then given by

$$u_2(\boldsymbol{\theta}) = t_*(\boldsymbol{\theta}) + i[t_* * \mathcal{F}(\phi)](\boldsymbol{\theta}) + O(\phi^2). \quad (6.21)$$

We see that the optimal solution $t_*(\boldsymbol{\theta})$ has been perturbed by an amount $i[t_* * \mathcal{F}(\phi)](\boldsymbol{\theta})$. On account of the convolution, each spatial frequency component of $\phi(\mathbf{r})$ will generate a scaled, translated copy of $t_*(\boldsymbol{\theta})$ centered at the corresponding coordinate in the image plane. The time-averaged effect of these “speckles” will degrade the contrast ratio, and the AO system must be designed to minimize the residual wavefront error within the spatial frequency passband of interest for planet detection.

6.4. Fourier Transform Wavefront Reconstruction

The results of the preceding subsection suggest that it may be useful to estimate and control the individual spatial frequency components of the wavefront aberration ϕ . In fact, performing the wavefront reconstruction in this basis has a number of additional advantages. Computational requirements are reduced to $O(n^2 \log n)$, where n is the 1-dimensional order of the AO system. Adaptive control algorithms can be easily implemented which adjust in real time to variations in the spatial and temporal spectra of atmospheric turbulence. Finally, it may be possible to further improve the performance of the system by implementing a predictive control algorithm which identifies and accounts for the velocity of the wind.

To illustrate the basic motivation for Fourier transform wavefront reconstruction, we re-write the basic WFS model given by Eq. (2.47) in the form

$$\begin{pmatrix} s^x(\mathbf{r}_{ij}) \\ s^y(\mathbf{r}_{ij}) \end{pmatrix} = \begin{pmatrix} (\chi * (\partial\phi/\partial x))(\mathbf{r}_{ij}) \\ (\chi * (\partial\phi/\partial y))(\mathbf{r}_{ij}) \end{pmatrix} + \begin{pmatrix} \eta^x(\mathbf{r}_{ij}) \\ \eta^y(\mathbf{r}_{ij}) \end{pmatrix}. \quad (6.22)$$

Here \mathbf{r}_{ij} denotes the coordinates of subaperture number i, j , and χ is the characteristic function of a subaperture centered at the point $(0, 0)$. *Neglecting aperture edge effects*, this formula may be transformed into the spatial frequency domain with the result

$$\begin{pmatrix} \mathcal{F}(s^x)(\boldsymbol{\kappa}) \\ \mathcal{F}(s^y)(\boldsymbol{\kappa}) \end{pmatrix} = 2\pi i \mathcal{F}(\chi)(\boldsymbol{\kappa}) \mathcal{F}(\phi)(\boldsymbol{\kappa}) \begin{pmatrix} \kappa_x \\ \kappa_y \end{pmatrix} + \begin{pmatrix} \mathcal{F}(\eta^x)(\boldsymbol{\kappa}) \\ \mathcal{F}(\eta^y)(\boldsymbol{\kappa}) \end{pmatrix} \quad (6.23)$$

Since both the wavefront sensor noise η^x and η^y and the phase error ϕ have spatially stationary statistics, the wavefront reconstruction task decouples into separate 2×1 dimensional problems at each spatial frequency. For example, the standard (transformed) pseudo-inverse estimator for the phase error takes the form

$$\widehat{\mathcal{F}(\phi)}(\boldsymbol{\kappa}) = \frac{\kappa_x \mathcal{F}(s^x)(\boldsymbol{\kappa}) + \kappa_y \mathcal{F}(s^y)(\boldsymbol{\kappa})}{2\pi i \mathcal{F}(\chi)(\boldsymbol{\kappa}) |\boldsymbol{\kappa}|^2}. \quad (6.24)$$

The computational complexity of the Fourier transform reconstructor can be seen to be $O(n^2 \log n)$, as opposed $O(n^4)$ for the explicit matrix-vector-multiply solution in the spatial domain.

Further discussion of the Fourier transform reconstructor is outside the scope of this survey. See [49, 50, 51] for further details and information on topics including (i) proper treatment of boundary conditions in the finite aperture case, (ii) adaptive optimization of the control bandwidth in closed-loop applications, and (iii) new work on predictive control algorithms which identify the wind velocity vector and anticipate the spatial translation of atmospheric turbulence across the wavefront sensor.

7. Summary

After a tutorial overview of astronomical AO, we presented four special topics that are of vital scientific importance and are amenable to inverse problems techniques.

The first special topic, laser guidestar AO, is motivated by the lack of sky coverage that can be obtained with natural light sources. Laser guidestar AO is essential for extremely large telescopes, but it gives rise to a number of complications, including the cone effect and the spot elongation problem. We presented a matched filtering scheme to deal with spot elongation.

The second topic, atmospheric turbulence tomography, has been proposed to deal with the cone effect and is of fundamental importance for emerging technologies like multi-conjugate AO and multi-object AO. We presented a detailed description of the implementation of the maximum a posteriori estimation technique for turbulence tomography.

Deformable mirror modeling and parameter identification, the third topic, is essential for multi-object AO and for proposed control schemes which do not rely on direct measurement-based feedback. We provided a detailed discussion of the implementation of adjoint techniques for parameter identification in the context of deformable mirrors.

The final topic, high contrast imaging, is required for the direct imaging of extraterrestrial planets. We included a mathematical description of an approach known as apodized pupil Lyot coronagraphy, and we discussed its algorithmic implementation.

A number of important and mathematically challenging topics were not presented in this review. These include modeling and parameter identification for the point spread functions that arise in AO-corrected imaging, the modeling and estimation of the dynamics of the turbulent atmosphere, and estimation problems that arise from innovative wavefront sensing techniques like pyramid sensing and phase diversity.

8. Acknowledgements

Ellerbroek gratefully acknowledges the support of the TMT partner institutions. They are the Association of Canadian Universities for Research in Astronomy (ACURA), the California Institute of Technology and the University of California. This work was supported as well by the Gordon and Betty Moore Foundation, the Canada Foundation for Innovation, the Ontario Ministry of Research and Innovation, the National Research Council of Canada, the Natural Sciences and Engineering Research Council of Canada, the British Columbia Knowledge Development Fund, the Association of Universities for Research in Astronomy (AURA) and the U.S. National Science Foundation.

Vogel received support through a grant from the Optical Sciences Company and from the National Science Foundation Science and Technology Center for Adaptive Optics, managed by the University of California at Santa Cruz under cooperative agreement No. AST-9876783.

9. References Cited

- [1] S. Adkins et al., "The design and optimization of detectors for adaptive optics wavefront sensing," in Proc. SPIE 6272, *Advanced in Adaptive Optics II*, B. Ellerbroek and D. Bonaccini, eds.,

- 62721E (2006).
- [2] F. Assemat et. al, "The FALCON concept: multi-object adaptive optics and atmospheric tomography for integral field spectroscopy", *MNRAS*, **376**, 287-312.
 - [3] H.T. Banks and K. Kunisch, *Estimation Techniques for Distributed Parameter Systems*, Birkhuser (1989).
 - [4] Horace Babcock, "The Possibility of Compensating Astronomical Seeing," *PASP* 65, 229-36 (1953).
 - [5] J. M. Beckers, "Increasing the size of the isoplanatic patch with multi-conjugate adaptive optics," in *Proceedings of European Southern Observatory Conference and Workshop on Very Large Telescopes and Their Instrumentation*, M. H. Ulrich, ed., Vol.30 of ESO Conference and Workshop Proceedings (European Southern Observatory, Garching, Germany, 1988), pp. 693-703.
 - [6] M. Booth, M. Neil, R. Jukaitis, and T. Wilson, "Adaptive aberration correction in a confocal microscope", *Proc Natl Acad Sci USA*, 99 (2002), pp. 57885792.
 - [7] C. Brezinski, *Computational Aspects of Linear Control (Numerical Methods and Algorithms)*, Springer, 2002.
 - [8] G. Brusa, A. Riccardi, F. P. Wildi, M. Lloyd-Hart, H. M. Martin, R. Allen, D. L. Fisher, D. L. Miller, R. Biasi, D. Gallieni, and F. Zocchi, "MMT adaptive secondary: first AO closed-loop results," in *Astronomical Adaptive Optics Systems and Applications*. Edited by Tyson, Robert K.; Lloyd-Hart, Michael, vol. 5169 of *Proc. SPIE*, pp. 26-36, Dec. 2003.
 - [9] J. Carroll, D.C. Gray, A. Roorda, and D. Williams, "Recent Advances in Retinal Imaging With Adaptive Optics", *Optics and Photonics News* 36 (2005)
 - [10] T. Chew, R. Clare, and R. Lane, "A comparison of the Shack-Hartmann and pyramid wavefront sensors," *Opt. Comm.*, **268** 189195 (2006).
 - [11] C. Dainty, "From Astronomy to the Consumer Market: today's industrial and medical application of adaptive optics", July/Aug 2007 issue of *Technology Ireland*.
 - [12] M.A. Davison, "The ill-conditioned nature of the limited angle tomography problem", *SIAM Journal of Applied Mathematics*, 43 (1983), pp. 428-448.
 - [13] J. Dawson et al., "Multi-watt 589nm fiber laser source," in *Proc. SPIE 6102, Fiber Lasers III*, A. Brown, J. Nilsson, D. Harter, and A. Tunnermann, eds., 61021F (2006).
 - [14] R. Dekany, M. Britton, D. Gavel, B. Ellerbroek, G. Herriot, C. Max, J.-P. Veran, "Adaptive optics requirements for TMT", *Proc. SPIE 5490*, pp. 879-890 (2004).
 - [15] C. Denman et al., "Characteristics of sodium guidestars created by the 50-watt FASOR and first closed-loop AO results at the Starfire Optical Range," in *Proc. SPIE 6272, Advances in Adaptive Optics II*, B. Ellerbroek and D. Bonaccini, eds., 62721L (2006)
 - [16] "Science with the European Extremely Large Telescope," <http://www.eso.org/sci/facilities/eelt/science/>, 2009.
 - [17] B.L. Ellerbroek, "Efficient computation of minimum-variance wave-front reconstructors with sparse matrix techniques," *J. Opt. Soc. Am. A*, 19, pp. 1803-1816 (2002).
 - [18] B.L. Ellerbroek and C.R. Vogel, "Simulations of closed-loop wavefront reconstruction for multiconjugate adaptive optics on giant telescopes", *Proc. SPIE 5169-23, Adaptive Optics System Technologies II* (2003), pp. 206-217.
 - [19] B. Ellerbroek, et al, "Progress towards developing the TMT AO systems and their components," in *SPIE Proc. 7015, "Adaptive Optics Systems"*, N. Hubin, P. Wizinowich, and C. Max, eds., 2008.
 - [20] R. Foy, et al., "ELPOA: toward the tilt measurement from a polychromatic laser guide star," in *Proc. SPIE 4007, Adaptive Optical Systems Technology*, P. Wizinowich, ed., 284 (2000).
 - [21] T. Fusco, et al., "Characterization of adaptive optics point spread function for anisoplanatic imaging. Application to stellar field deconvolution," *Astron. Astroph. Suppl. Ser.* **142**, 149-56 (1999).
 - [22] A. M. Ghez, et. al., "Full Three Dimensional Orbits for Multiple Stars on Close Approaches to the Central Supermassive Black Hole", *Astron. Nachr.* **324**, 2003.
 - [23] L. Gilles, "closed-loop stability and performance analysis of least-squares and minimum-variance control algorithms for multi-conjugate adaptive optics," *Applied Optics* 44, pp. 993-1002 (2004).
 - [24] L. Gilles, B. L. Ellerbroek, and, C. R. Vogel, "Preconditioned conjugate gradient wave-front reconstructors for multi-conjugate adaptive optics, *Applied Optics*, 42, 5233-5250 (2003).
 - [25] L. Gilles and B. Ellerbroek, "Shack-Hartmann wavefront sensing with elongated sodium laser beacons: centroiding versus matched filtering," *Appl. Opt.* **45**, 6568 (2006).
 - [26] L. Gilles and B.L. Ellerbroek, "Split atmospheric tomography using laser and natural guide stars", *JOSA A*, Vol. 25 Issue 10, pp.2427-2435 (2008).

- [27] G. Golub and C. VanLoan, *Matrix Computations, 2nd Edition*, Johns Hopkins University Press, 1989.
- [28] “GMT Science Case and Technical Requirements,” <http://www.gmto.org/sciencecase>, 2009.
- [29] J. Goodman, *Introduction to Fourier Optics*, McGraw-Hill, 1996.
- [30] J. Gourlay, T. Yang, M. Ishikawa, and A. C. Walker, “Low-order adaptive optics for free-space optoelectronic interconnects,” *Applied Optics*, 39 (2000), pp. 714720.
- [31] G. Hale, *Study of Stellar Evolution*, 1908.
- [32] J.W. Hardy, *Adaptive Optics for Astronomical Telescopes*, Oxford University Press, 1998.
- [33] C.L. Hom, P.D. Dean, and S.R. Winzer, “Simulating electrostrictive deformable mirrors: I. Nonlinear static analysis”, *Smart Material and Structures*, 8 (1999), pp. 691-699.
- [34] *J. Opt. Soc. Am.* **66** issue 3, 1976.
- [35] *J. Opt. Soc. Am. A* **11** issues 2-3, 1994.
- [36] E. Kibblewhite, “Calculation of returns from sodium beacons for different types of laser Kibblewhite,” in *Proc. SPIE 7015, Adaptive Optics Systems*, N. Hubin, C. Max, and P. Wizinowich, eds., 70150M-70150M-9 (2008).
- [37] O. Lardiere, et al., “Laser-guide-star wavefront sensing for TMT: experimental results of the matched filtering,” in *Proc. SPIE 7015, Adaptive Optics Systems*, Hubin, Norbert, Max, Claire E., and Wizinowich, Peter L. eds., pp. 70154T-70154T-12 (2008).
- [38] W. Latham, and W. Tilton, “Calculation of prolate functions for optical analysis,” *Appl. Opt.* **26**, 2653–2658 (1987).
- [39] Soummer, R., “Apodized Pupil Lyot Coronagraphs for Arbitrary Telescope Apertures,” *ApJ* **618**, 161-164 (2005).
- [40] M. Liu, “Astronomical Science with Laser Guide Star Adaptive Optics,” in *Proc. SPIE 6272, Advances in Adaptive Optics II*, B. Ellerbroek and D. Bonaccini, eds., 2006.
- [41] B. Lyot, “The Study of the Solar Corona and Prominences with Eclipses,” *MNRAS* 99, 580-94 (1939).
- [42] B. Macintosh, “The Gemini Planet Imager,” in *Advances in Adaptive Optics II*, Ellerbroek, B. and Domenico, D. eds., *Proc. SPIE*, **6272** 62720L (2006).
- [43] R.B. Makidon, A. Sivaramakrishnan, M.D. Perrin, L.C. Roberts, B.R. Oppenheimer, R. Soummer, and J.R. Graham, “An analysis of fundamental waffle mode in early AEOS adaptive optics images”, *Astronomical Society of the Pacific*, 117 (2005) pp. 831846.
- [44] F. Marchis, et.al., “Keck AO survey of Io global volcanic activity between 2 and 5 m”, *Icarus* **176**, 2005.
- [45] C. Marois, et al., “Direct Imaging of Multiple Planets Orbiting the Star HR 8799,” *Science*, Nov. 13, 2008.
- [46] K.M. Morzinski, J.W. Evans, S. Severson, B. Macintosh, D. Dillon, D. Gavel, C. Max, and D. Palmer, “Characterizing the potential of MEMS deformable mirrors for astronomical adaptive optics”, *Proc. SPIE* **6272** 627221 (2006).
- [47] I. Newton, *Opticks*, 1730.
- [48] R. Paxman, T. Schulz, and J. Fineup, “Joint estimation of object and aberrations by using phase diversity” *J. Opt. Soc. Am. A* **9** (1992), pp. 1072-1085.
- [49] L. A. Poyneer, “Advanced techniques for Fourier transform wavefront reconstruction,” *Proc. SPIE 4839, Adaptive Optical System Technologies II*, Wizinowich, Peter L. and Bonaccini, Domenico, eds., pp. 1023-1034 (2003).
- [50] Lisa A. Poyneer and Jean-Pierre Vran, “Optimal modal Fourier-transform wavefront control,” *J. Opt. Soc. Am. A* **22**, 1515-1526 (2005).
- [51] L.A. Poyneer, B. Macintosh, and J.-P. Veran, “Fourier transform wavefront control with adaptive prediction of the atmosphere”, *JOSA A*, Vol. 24 Issue 9, pp.2645-2660 (2007).
- [52] A. Riccardi, G. Brusa, M. Xompero, D. Zanotti, C. Del Vecchio, P. Salinari, P. Ranfagni, D. Gallieni, R. Biasi, M. Andrichetoni, S. Miller, P. Mantegazza, “The adaptive secondary mirrors for the Large binocular telescope,” in *Advancements in Adaptive Optics*. Edited by D. Bonaccini-Calia, B. L. Ellerbroek, R. Ragazzoni, vol. 5490 of *Proc. SPIE*, pp. 1564-1571, Jun. 2004.
- [53] F. Roddier, *Adaptive Optics in Astronomy*, Cambridge University Press, 1999.
- [54] M. Roggemann and B. Welsh, *Imaging Through Turbulence*, CRC Press, 1996.
- [55] R. Sasiela, *Electromagnetic Wave Propagation in Turbulence : Evaluation and Application of Mellin Transforms, 2nd Edition*, SPIE, 2007.
- [56] A. Sivaramakrishnan, et al., “Sensing Phase Aberrations Behind Lyot Coronagraphs,” *ApJ* **688** 701–708 (2008).
- [57] Y. Saad, *Iterative Methods for Sparse Linear Systems, 2nd Edition*, Society of Industrial and Applied Mathematics, Philadelphia, 2003.

- [58] J.-C. Siquin, J.-M. Luron, and C. Guillemard, “Deformable mirror technologies for astronomy at CILAS”, Proc. SPIE **7015** 7015-23 (2008).
- [59] J.B. Stewart, A. Doiuf, Y. Zhou, T.G. Bifano, “Open-loop control of a MEMS deformable mirror for large-amplitude wavefront control”, Journal of the Optical Society of America-A, **24** (2007), pp. 3827-3833.
- [60] S. Timoshenko and S. Woinowsky-Krieger, *Theory of Plates and Shells*, McGraw-Hill, 1976.
- [61] “Thirty Meter Telescope Detailed Science Case,” <http://www.tmt.org/foundation-docs/TMT-DSC-2007-R1.pdf>, 2007.
- [62] U. Trottenberg, C. Oosterlee, and A. Schuller, *Multigrid*, Elsevier, 2001.
- [63] C.R. Vogel, *Computational Methods for Inverse Problems*, Society of Industrial and Applied Mathematics, Philadelphia, 2002.
- [64] C.R. Vogel, D.W. Arathorn, A. Roorda, and A. Parker, “Retinal motion estimation in adaptive optics scanning laser ophthalmoscopy”, Optics Express, **14** (2006), pp. 487-497.
- [65] C.R. Vogel and Q. Yang, “Modelling, simulation, and open-loop control of a continuous facesheet MEMS deformable mirror”, Journal of the Optical Society of America-A, **23** (2006), pp. 1074-1081.
- [66] C.R. Vogel and Q. Yang, “Modelling and open-loop control of point-actuated, continuous facesheet deformable mirrors”, SPIE 6272-73, Advancements in Adaptive Optics II (2006).
- [67] K. Wallace, et al., “Postcoronagraph wavefront sensing for the Gemini Planet Imager,” Proc. SPIE 7015-243 (2008).
- [68] Q. Yang, C. Vogel, and B. Ellerbroek, “Fourier domain preconditioned conjugate gradient algorithm for atmospheric tomography”, Applied Optics, Vol. 45 Issue 21, pp.5281-5293 (2006).